Structural Damage Localisation Through Shaped Inputs

AALBORG UNIVERSITY
STUDENT REPORT

M.Sc. Mechanical Design
Lasse B. Klockmann & Palle H. Veis
07-06-2018

TITLE PAGE

Project title:
Structural Damage Localisation
Through Shaped Inputs

University:
Aalborg University Esbjerg

Supervisors:
Lars Damkilde &
Martin Dalgaard Ulriksen

Assistant supervisor:
Bilal Ali Qadri

Period:
01.09.2017 to
07.06.2018

Number of pages:
Report: 60 pages
Appendix: 10 pages

Authors:

Lasse Bolther Klockmann

Palle Høgh Veis

Abstract

The present thesis explores a newly proposed method, the Shaped Damage Locating Input Distribution (SDLID) scheme, for vibration-based damage identification localisation. The premise of the method is as follows: Given a structure is suffering from any type of damage, the steady-state vibration response, when applying the same load distribution, will be identical to that of the undamaged structure if the damage is rendered dormant. Based on this principle, the SDLID method operates by designing shaped inputs, which suppress certain steady-state vibration quantities. Damage is localised when the vibration signature from a damaged and undamaged structure, induced by the same shaped inputs, corresponds. Besides a numerical validation of the method, an examination regarding practical implementation is made by introducing experimental analyses of a six-story frame structure.

PREFACE

This master thesis is made by group BM3-3-E17 on the M.Sc. programme in Mechanical Design at Aalborg University Esbjerg, in the period from September 1st, 2017 to June 7th, 2018.

Detecting and localising damages in structures are of major interest, primarily of economic and safety reasons. Consequently, damage detection and localisation methods have been developed and tested through time. It is the opinion of the authors that sufficient evidence exists to promote the use of vibration data for damage detection, whereas damage localisation yet must be proven on real-life-problems. Most localisation methods rely on system identification, which for real-life problems often can be hard to obtain with sufficient accuracy. The purpose of this master thesis is to investigate a newly proposed method utilizing shaped damage locating input distribution (SDLID) for localising structural damages, without the use of system identification. The idea and theory behind the SDLID method will be described and validated. This includes experiments on a frame structure in a laboratory environment.

This master thesis has been made under the supervision of Professor Lars Damkilde, Ph.D. fellow Martin D. Ulriksen and Research Assistant Bilal A. Qadri, whom the authors would like to thank. The authors would also like to thank Jan Á. Nikolajsen and Peter R. Lauridsen for their guidance during the project and to Jan E. Andersen for help with the laboratory setup.

A 3D finite element method (FEM)-program has been developed in MATLAB to establish and calibrate a mathematical model of the frame structure and designing shaped inputs used to localise damage in experimental work. It is presumed that the reader is familiar with the FEM and vibration analysis.

References and appendices are indicated with respectively [#] and Appendix X. An overview of the references can be found at the end of the report.

Table of content

1 INTRODUCTION

This chapter describes the motivation for structural health monitoring (SHM), followed by a brief description of existing approaches and a newly proposed method for damage localisation.

1.1 MOTIVATION FOR MONITORING STRUCTURAL INTEGRITY

In engineering societies, monitoring structures to detect, localise and assess damage has always been of interest, since it can increase safety and reduce maintenance costs by pin-pointing when and where to search for damages. A long-term perspective is ongoing monitoring of a structure's integrity, thereby preventing sudden failures. If the monitoring provides sufficient preventive safety, it could lead to lower consumption of materials by reducing design safety factors.

When designing structures ensuring functionality and integrity during normal operation is crucial. This includes adding safety factors in various parts of the design process such as material parameters and loads. Structures' legal requirements, and usually also specific industry standards (i.e. DNVGL standards), must be fulfilled. These requirements are continuously being modified, sometimes due to experiences from accidents like the collapse of Alexander Kielland, illustrated in Figure 1-1, which supposedly collapsed due to human errors [1]. These errors are believed to have resulted in crack initiating in brace D-6, see Figure 1-1, that lead to collapse of the remaining five braces and thereby leg D, resulting in the capsize and sinking of the platform [1].

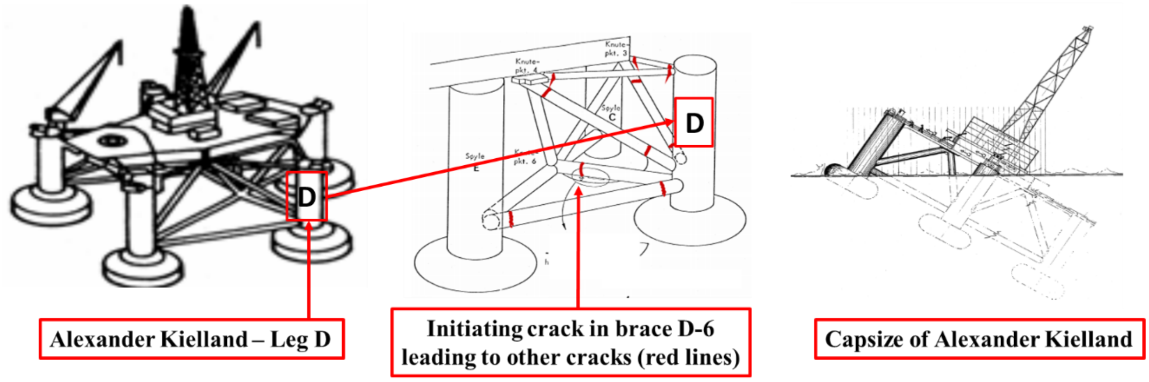

Figure 1-1: Illustrating steps in the sinking of platform Alexander Kielland [2].

The economic perspective in designing structures is to fulfil above mentioned requirements and giving the best compromise between functionality, expected lifetime and total cost. Even though a structure is designed according to above requirements, avoiding damages in practice is often troublesome and, in some cases, almost impossible, since damage occur from accidents, environmental conditions and human errors. In present thesis damage is defined as a change (perturbation) in a system's mass or stiffness.

Stiffness damages often develop in locations where stress concentrations accumulate, for example from geometry changes or weldings, and will in worst case scenarios result in cracks and structures collapsing. An example of a mass-related damage could be an offshore structure exposed to marine growth, see Figure 1-2b. The extra mass contribution from marine growth will lower the eigenfrequencies of the structure.

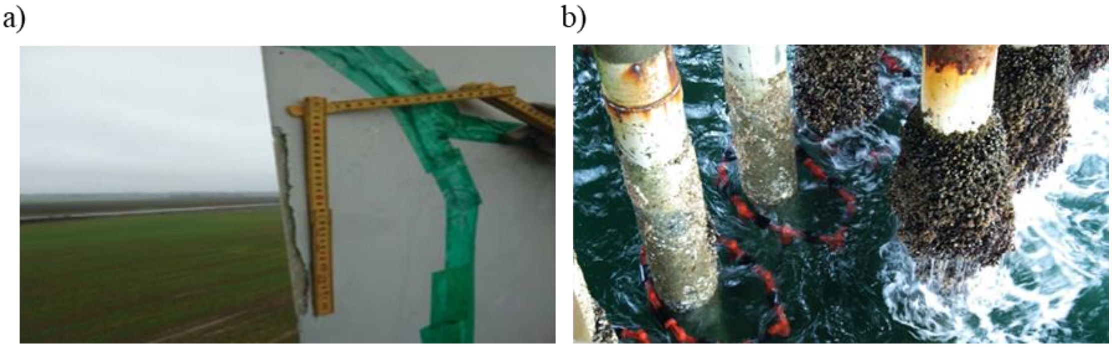

Figure 1-2: Example of stiffness and mass damage. a) Crack in wind turbine blade resulting in a stiffness damage [3]. b) Marine growth on an offshore structure resulting in a mass damage [4].

An early detection of a damage improves the possibility for repairing to avoid catastrophes, like Alexander Kielland. One way of reducing failure rates is done by a more thorough follow-up on the production processes. This is resource demanding and still leaves the risk of eventual interferences occurring after each production/installation process.

The oil industry has since the 1970's been eager on developing a method for monitoring structures, and thereby detecting damages, through vibration-based damage detection methods [5]. For offshore structures this could lower costs and minimise the need for visual inspections. In the early 1980's the oil industry largely abandoned the search of a vibration-based damage detection method, due to practical problems like changing mass from varying fluid levels, marine growth and the inability to excite higher modes [5].

Since the late 1970's the aerospace community has had focus on vibration-based damage detection and localisation methods [5]. This could be for use in aeronautics, where visual inspections can be very difficult or even impossible since cracks can develop in the inner plates of a wing [5].

The civil engineering community also has interest in vibration-based damage detection and localisation methods. One example is bridges, where non-visible damages can be detected at an early stage or for securing the structural integrity of the bridge [5].

In the mechanical engineering societies, besides detection, the task of locating damages has also been of major interest. Damage localisation methods, without resource-demanding visual inspections, have been sought for many years. Many industries, and especially the offshore industry, has focus on operation time and maintenance costs. Therefore, many studies, using different methods, have been performed in the attempt to facilitate remote structural health monitoring [5].

The safety and economic perspective when designing structures leaves it desirable to find a method for detecting and localising damages, with a low demand on resource and cost.

1.2 STRUCTURAL HEALTH MONITORING

SHM stands as an alternative method to perform non-destructive testing that could prevent accidents by identifying structural damage before it leads to failure. One of the major advantages using SHM is that it can search for damage globally on the structure, where manual inspection is a local procedure.

As stated in Section 1.1, using SHM to detect, and locate, damages at its earliest possible stage is of interest in many industries. Since this can contribute to increasing safety against failure and prolonging the lifetime of structures, by giving relatively safe estimates of their ongoing integrity. Using SHM provides the ability to detect and locate damage at inaccessible areas, for example; internal voids or cracks, damage beneath surface treatment or marine growth. From an overall point of view vibration-based damage identification analysis can be categorised into the four levels stated below, where each new level presumes the previous is fulfilled [6]:

1. Detection of the damage
2. Localisation of the damage
3. Quantification of the damage
4. Assessment of consequence from the damage

Detection and localisation can be done in several ways, where two commonly used methods are manual (visual) or vibration-based analysis. Visual inspection can be a reasonable method to inspect for damage, if the structure has a relatively small, simple and open geometry. Since drones with attachable cameras have become easily accessible, visual inspection has become less resource demanding [7]. Though this method still leaves the lack of detecting hidden damages, for example cracks beneath corrosion protection or in the inner parts of a structure, hence this method is not discussed further in present thesis.

1.2.1 Basic Principles of Damage Detection and Localisation

To present the field of SHM, the following section elaborates on some existing damage detection and localisation methods.

It is believed that visual inspection for damages always has existed, whereas acoustic-based detection of damage in its most simple, and probably earliest, form is sound recognition. An example is checking for defects via a “hollow sound” when knocking on tiles, and it is believed to have existed since man has used tools [5].

1.2.2 Changes in Frequencies

Vandiver proposed a method for damage detection by looking at the changes in the eigenfrequencies of the structure when suffering from damages [8]. The experiments showed that when introducing damage to their structures, almost all scenarios showed a change in eigenfrequency. Although damages can be detectable in looking at the changes in a structure’s eigenfrequencies, this method heavily relies on relatively large damages. This was proven by Kenley and Dodds [8] who stated that before damage detection was possible using the eigenfrequencies, the damage, in this case, must produce at least 5% change in overall stiffness to overcome changes from environmental conditions.

Furthermore, they pointed out the importance in looking at the mode shapes belonging to the respective eigenfrequencies when trying to locate damages [8].

1.2.3 Changes in Mode Shapes

Yuen [8] proposed a damage localisation method using the changes in mode shapes:

$$\boldsymbol{\phi}_i^* = \frac{\boldsymbol{\phi}_i^d}{\omega_i^d} - \frac{\boldsymbol{\phi}_i^u}{\omega_i^u} \tag{1.1}$$

Where:

$\boldsymbol{\phi}^*$	the change in mode shapes
$\boldsymbol{\phi}^d$, $\boldsymbol{\phi}^u$	mode shapes for the damaged and undamaged state
$\boldsymbol{\omega}^d$, $\boldsymbol{\omega}^u$	eigenfrequencies for the damaged and undamaged state

These changes were computed introducing stiffness perturbation in each structural element for a numerical model, and later compared with measured changes to determine the damage location [8]. The method requires system identification[1] since the mode shapes for the damaged and undamaged state must be computed. Osegueda also performed a study [8], examining changes in dynamic properties of an offshore structure introduced to damage. In this study mode shapes could not be corelated with damage.

1.2.4 Stiffness Error Matrix

This method is based on the computation of an error matrix, between an undamaged and damaged system, where flexibility perturbation is introduced. For this method the flexibility matrix is calculated using following formula:

$$\boldsymbol{G_f} = \boldsymbol{K}^{-1} \tag{1.2}$$

Where:

$\boldsymbol{K}$	stiffness matrix

He and Ewins [8] presented the stiffness error matrix for damage identification, where the changes in the flexibility matrix could work as a damage detection/localisation method, hence:

$$\boldsymbol{E} = \boldsymbol{K^u} \Delta \boldsymbol{G_f} \boldsymbol{K^u} \tag{1.3}$$

Where:

$\boldsymbol{E}$	stiffness error matrix
$\boldsymbol{K^u}$	undamaged stiffness matrix
$\Delta \boldsymbol{G_f}$	difference in flexibility of a damaged and undamaged system

---

[1] System identification is a method for constructing a mathematical model of dynamical systems based on measured data.

Furthermore, the research showed that the stiffness error matrix contained more information than the mass error matrix when localising stiffness damages, hence Eq. (1.3) is more widely used [8].

1.2.5 Dynamic Damage Locating Vector

Bernal [9] proposed a theorem that connects changes in the transfer matrix to locate stiffness related damages. The theorem states that the null space of ΔG, which is the change in the transfer matrix, contains vectors that are Laplace transforms of dynamic excitations, which will create zero stresses at the damaged region. Given the physical domain Ω_D and a history of loads, $f(t)$, acting on specific coordinates, q, with $\sigma_D(t)$ being the associated stress field over Ω_D. The dynamic damage locating vector (DDLV) method states that if $f(t)$ is such that the stress field $\sigma_D(t) \equiv 0$ then following equation is valid:

$$\mathcal{L}\big(f(t)\big) = Null(\Delta\boldsymbol{G}) \cdot \nu \tag{1.4}$$

Where:

$\Delta\boldsymbol{G}$	change in the transfer matrix
ν	is arbitrary

The DDLV method does not forbid zero stresses over undamaged elements, hence this could be problematic when localising damages. Furthermore, the DDLV method does not circumvent system identification.

Aforementioned methods, regarding damage detection and localisation, have their pros and cons. In the next section, the Shaped Damage Locating Input Distribution (SDLID) method will be introduced as a new alternative for damage localisation avoiding system identification, which, in some cases, is troublesome to achieve with sufficient accuracy in an experimental context.

1.3 THE SHAPED DAMAGE LOCATING INPUT DISTRIBUTION METHOD

This thesis investigates the SDLID method for localising structural damages, assuming damage detection has taken place a priori [10].

The idea behind the method is to shape inputs at certain locations, such that specific steady-state vibration quantities are suppressed one location at a time. The damage is located when the vibration signature of the damaged structure corresponds with the vibration signature of the undamaged/reference structure, providing the merits of:

- circumventing system identification
- robustness against noise[2]
- low demand on sensors

---

[2] Since the SDLID method circumvents system identification robustness against signal noise increases.

The advantage of circumventing system identification is achieved, since only the vibration signatures (output) are compared. This is a relatively large advantage, since accurate system identification can be hard to obtain in practice [5].

The drawback of the SDLID method is primarily the demand for applying multiple controllable shaped inputs. Secondly, it is highly dependent on an accurate finite element (FE)-model of the undamaged/reference structure, which is used to design the shaped inputs [10]. A more thorough explanation of the theory behind the method is given in Section 2.4.

Since the SDLID method only has been tested using simple numerical examples, this thesis' main contribution is:

- Numerical and experimental exploration of the SDLID scheme

To realise this contribution, the following secondary contributions have been established:

- Erection of a 3D frame structure in the laboratory for static and dynamic testing
- Development of a 3D beam finite element method (FEM)-program in MATLAB with an optimization algorithm for model calibration and updating

The frame structure, which the experiments are performed on, is illustrated in Figure 1-3. For the purpose of this thesis the frame structure is constructed from aluminium beam elements and the joints are constructed with the components depicted in Figure 3-2 and further elaborated in Section 3.2. All components are from MakerBeam [11], except the treaded rods which are made in the laboratory at Aalborg University Esbjerg.

1.4 THESIS OUTLINE

The aim of present thesis is to conduct vibration-based damage identification on the frame structure, depicted in Figure 1-3, and numerical exploration of stiffness and mass perturbation localisation using the SDLID method. Due to project limitations the damage identification only includes level 1 and 2, namely detection and localisation, and the frame structure will only be subjected to mass perturbations in various locations.

Figure 1-3: Frame structure on top of I-profile used for fixation.

2 BACKGROUND THEORY

This chapter elaborates on the different theories used in this thesis regarding linear vibration analysis, finite element analysis, basic principles of damage localisation, the SDLID method and implementation of perturbations in an FE-model.

2.1 LINEAR VIBRATION THEORY

This section presents the fundamental theory of linear vibration analysis of multiple-degrees-of-freedom (MDOF) systems. The governing equation used to express a linear and time invariant system is known as the equation of motion:

$$\boldsymbol{M}\ddot{\boldsymbol{x}}(t) + \boldsymbol{C}\dot{\boldsymbol{x}}(t) + \boldsymbol{K}\boldsymbol{x}(t) = \boldsymbol{f}(t) \tag{2.1}$$

Where $\boldsymbol{M}$, $\boldsymbol{C}$ and $\boldsymbol{K}$ are the mass, damping and stiffness matrices of the system while $\ddot{\boldsymbol{x}}$, $\dot{\boldsymbol{x}}$ and $\boldsymbol{x}$ are the acceleration, velocity and displacement response with respect to time, t, and $\boldsymbol{f}$ is the force vector.

2.1.1 Modal Analysis

When describing a system's dynamic behaviour, the modal parameters, eigenfrequencies, mode shapes and damping ratios, are of major interest. Here the eigenfrequencies are an important parameter to establish, since they control which load frequencies the system can be exposed to without entering a resonance state. To obtain these modal parameters, the eigenvalue problem of an undamped system ($\boldsymbol{C}$ is assumed to be 0) is solved:

$$\left(\boldsymbol{K} - \omega_{0,i}^2\boldsymbol{M}\right)\boldsymbol{\phi_i} = \boldsymbol{0} \tag{2.2}$$

Since $\det\left(\boldsymbol{K} - \omega_{0,i}^2\boldsymbol{M}\right) = \boldsymbol{0}$, only non-trivial solutions are selected ($\boldsymbol{\phi}_i \neq \boldsymbol{0}$), the eigenfrequency, $\omega_{0,i}$, and eigenvector, $\boldsymbol{\phi}_i$, can be computed for each i$^{\text{th}}$ mode, respectively [12].

2.1.2 The Laplace Domain

This thesis includes experimental analysis of a structure's responses generated by harmonic loads from actuators. Various integral transforms exist to solve for, $\ddot{\boldsymbol{x}}$, $\dot{\boldsymbol{x}}$ and $\boldsymbol{x}$ in Eq. (2.1), for harmonic loaded MDOF systems. Following section presents a brief elaboration of the transformation into the Laplace domain used in present thesis.

The Laplace transform is an integral transform for solving linear differential equations [12]. The definition of a Laplace transform of a function $f(t)$ is:

$$\mathcal{L}\big(f(t)\big) = \int_0^\infty f(t)e^{-st}dt \tag{2.3}$$

The Laplace transform changes the domain of f from the time domain to the complex domain, where s is a complex variable consisting of a real and imaginary part:

$$s = a + j\omega \tag{2.4}$$

Where:

a	is the real part
ω	frequency
j	imaginary unit

This domain can also be illustrated visually, with the real part following the first axis, and the imaginary part along the second axis, see Figure 2-1.

Solving the roots for the homogenous part of Eq. (2.1) and assuming classical damping yield:

$$\lambda_{i,i+1} = -\zeta_i \omega_{0,i} \pm \omega_{d,i} j \tag{2.5}$$

Where (for the i^{th} mode):

ζ_i	damping ratio
$\omega_{d,i}$	damped eigenfrequency
$\omega_{0,i}$	undamped eigenfrequency

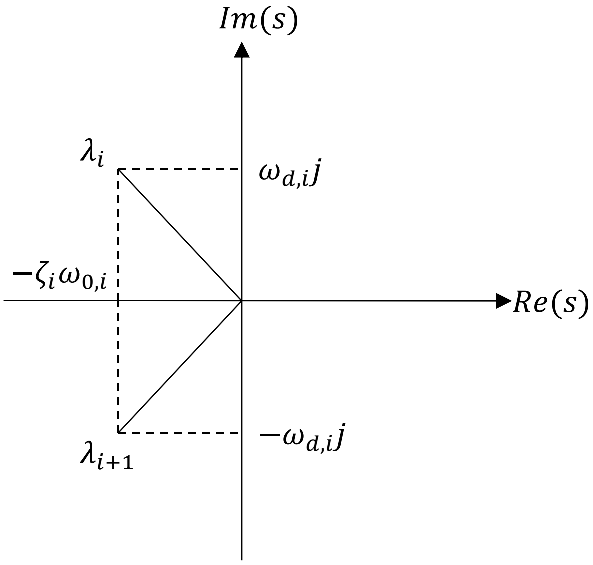

Figure 2-1: Location of roots of the equation of motion in the complex domain for an under-critically damped system.

The real part, a, produces exponential functions depending on its value. When the roots of a system have a positive real part, the system becomes unstable and will be located at the right side of the imaginary axis. Correspondingly, the system will become stable when $a < 0$.

Taking the Laplace transformation of Eq. (2.1) turns the differentiation and integration into division and multiplication. As illustrated in Figure 2-2, the system $g(t)$ provides a linear mapping between the input, $f(t)$, and output, $x(t)$.

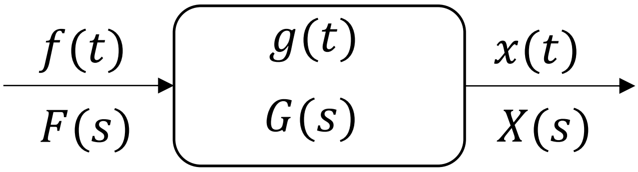

Figure 2-2: Illustration of the linear relationship between the input and output of a LTI-system in the time and complex domain respectively.

Taking the Laplace transform of Eq. (2.1) with zero initial conditions yields [12]:

$$(\boldsymbol{M}s^2 + \boldsymbol{C}s + \boldsymbol{K})\boldsymbol{X}(s) = \boldsymbol{F}(s) \tag{2.6}$$

Where:

$\boldsymbol{X}(s)$	complex response vector
$\boldsymbol{F}(s)$	complex force vector

Reworking Eq. (2.6) yields the transfer function $\boldsymbol{G}(s)$:

$$\boldsymbol{X}(s) = (\boldsymbol{M}s^2 + \boldsymbol{C}s + \boldsymbol{K})^{-1}\boldsymbol{F}(s) = \boldsymbol{G}(s)\boldsymbol{F}(s) \tag{2.7}$$

Here it is obvious that instead of operating with a second order ordinary differential equation, using the Laplace transformation allows to compute a solution to the response using simple multiplication. When the desired response, $\boldsymbol{X}(s)$, is obtained, the inverse Laplace transformation is used to bring the solution back to the time domain, hence if this is necessary:

$$\mathcal{L}^{-1}\big(\boldsymbol{X}(s)\big) = \boldsymbol{x}(t) \tag{2.8}$$

In present thesis, the SDLID scheme is formulated in the Laplace domain to ease the computation of the shaped inputs used for the numerical and experimental analyses.

2.2 FINITE ELEMENT METHOD

The frame structure used for the laboratory test is constructed of MakerBeam aluminium beam elements and is illustrated in Figure 2-3. The relative slender and open profile of the individual beam elements leads to the assumption that shear forces are negligible, hence a FE-model on basis of Bernoulli-Euler beam theory is chosen. Detailed modelling of the connection, depicted in Figure 3-1b, is omitted in present thesis. Alternatively, rotational springs are incorporated into the FE-model to compensate this, which is elaborated in Section 4.3.

This section presents the fundamental theory behind the FEM. Further elaboration on the principles of a Bernoulli-Euler beam element in 2D is found in Appendix B [13].

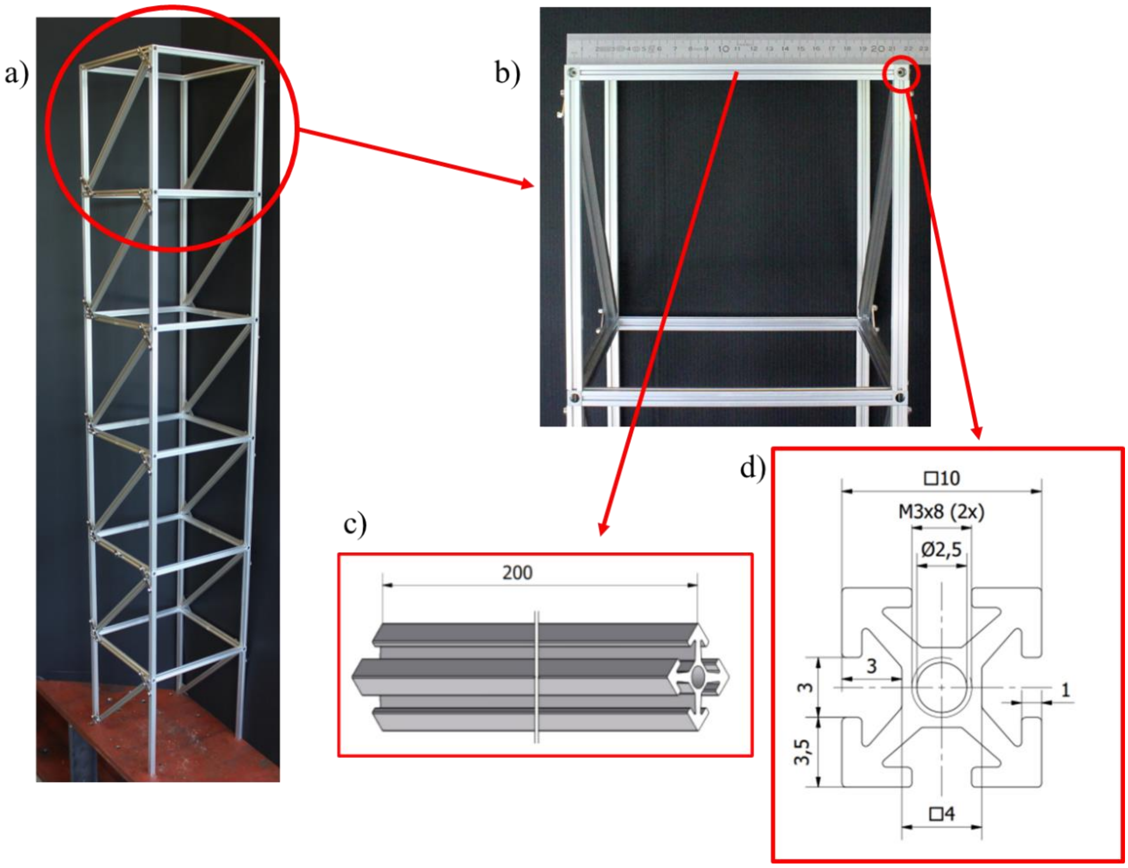

Figure 2-3: a) Frame structure.
b) Magnification of the upper floor, illustrating beam length vs. cross section size.
c) Blueprint of beam. d) Blueprint of beam cross section [14].

2.2.1 FE-Modelling of Real-Life Structure

The three steps in representing a real-life structure as an FE-model are:

- Classification
- Modelling
- Discretization

These steps are performed to convert the real-life characteristics into a mathematical model.

Classification is identifying if the problem can be treated as static, dynamic, linearly and time dependent. It also involves the trade-off between requested accuracy and consumption of resources.

Modelling is converting the essentials of the real-life structure/system into a mathematical model. Examples of assumptions: simplifying into 2D, determining boundary conditions and deciding element type.

Discretization is dividing the mathematical model into a finite number of elements and deciding element type. Choosing number and type of elements is a trade-off between accuracy and resources.

Converting the frame structure into a mathematical model is done by implementing a node at the fixations and each connection. Furthermore, each MakerBeam, apart from the braces, is divided into two elements, giving a discretized model as depicted in Figure 2-4a.

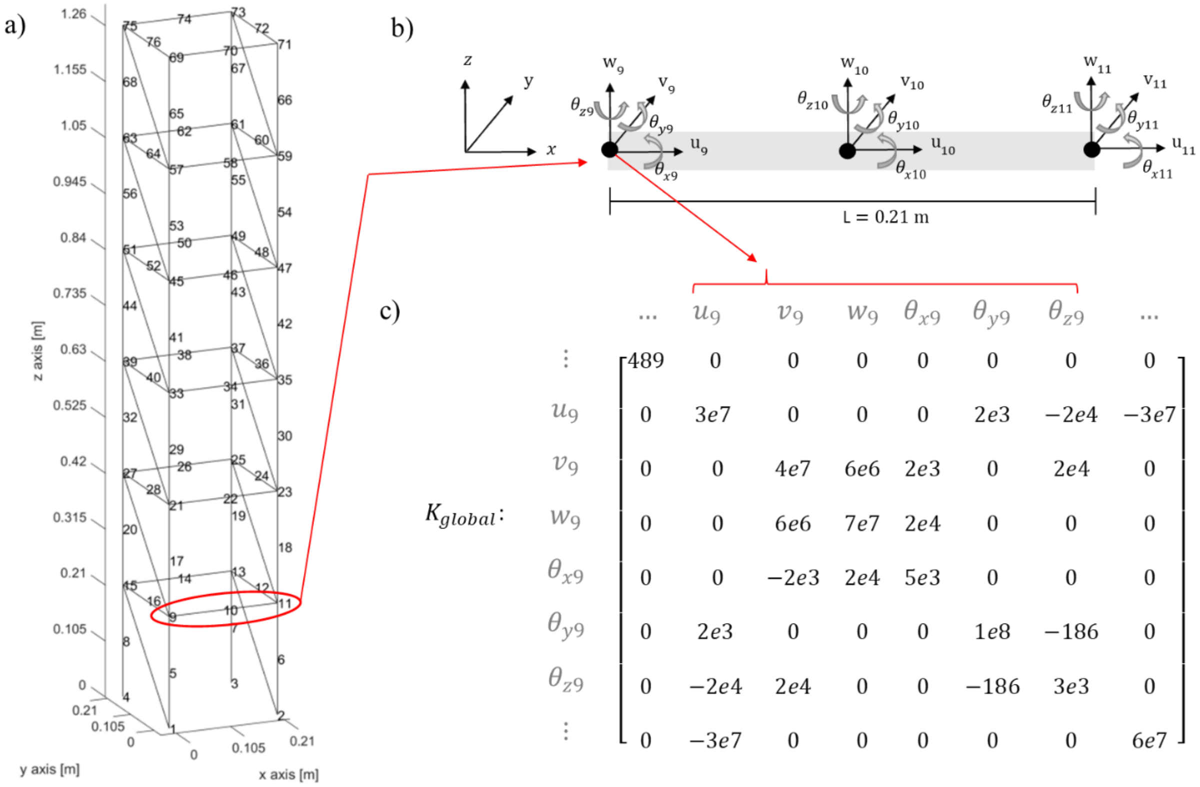

$$K_{global}: \begin{array}{c|cccccccc} & \cdots & u_9 & v_9 & w_9 & \theta_{x9} & \theta_{y9} & \theta_{z9} & \cdots \\ \vdots & 489 & 0 & 0 & 0 & 0 & 0 & 0 & 0 \\ u_9 & 0 & 3e7 & 0 & 0 & 0 & 2e3 & -2e4 & -3e7 \\ v_9 & 0 & 0 & 4e7 & 6e6 & 2e3 & 0 & 2e4 & 0 \\ w_9 & 0 & 0 & 6e6 & 7e7 & 2e4 & 0 & 0 & 0 \\ \theta_{x9} & 0 & 0 & -2e3 & 2e4 & 5e3 & 0 & 0 & 0 \\ \theta_{y9} & 0 & 2e3 & 0 & 0 & 0 & 1e8 & -186 & 0 \\ \theta_{z9} & 0 & -2e4 & 2e4 & 0 & 0 & -186 & 3e3 & 0 \\ \vdots & 0 & -3e7 & 0 & 0 & 0 & 0 & 0 & 6e7 \end{array}$$

Figure 2-4: a) Discretization of frame structure with corresponding node numbers.
b) Magnification of a MakerBeam with node no. 9, 10 & 11, with respective DOF.
c) Section of global stiffness matrix showing DOF from node no. 9.

In Figure 2-4b, a single MakerBeam is magnified showing its respective degrees-of-freedom (DOF). A part of the global stiffness matrix is depicted in Figure 2-4c, where the DOF from node no. 9 are implemented. The global stiffness matrix is constructed by assembling local stiffness matrices which are rotated into a global coordinate system. A brief derivation on calculation of local stiffness, mass and rotation matrices and assembling into global matrices are in Appendix B.

2.3 Implementation of Perturbation in FE-model

To conduct a numerical exploration of the SDLID scheme, a perturbation must be implemented in an FE-model to facilitate damage localisation. This section explains how the stiffness and mass perturbation of the structure are implemented in the numerical model and the assumptions that have been made.

2.3.1 Mass Perturbation

To simulate an added mass, for example marine growth on offshore structures, a perturbation must be implemented in the mass matrix. In this thesis, a consistent mass matrix is used for the FEM-program, since this is proven to be more accurate than a lumped mass matrix [13]. To illustrate the procedure in implementation of a mass perturbation, the system in Figure 2-5 is used as an example, where the perturbation is located in node 1.

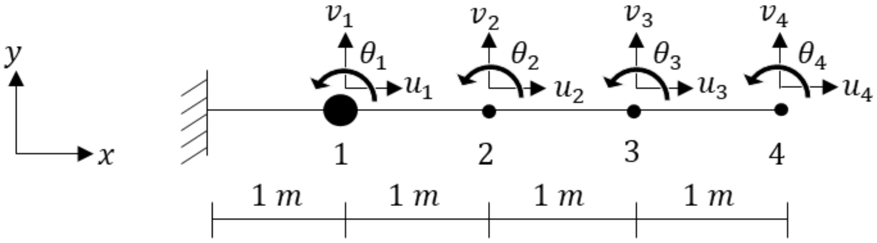

Figure 2-5: 2D beam elements with a fixed support.

The mass perturbation implementation of a size ψ is done for the vertical and horizontal DOF in the mass matrix for node 1. In Eq. (2.9) an example of implementation for the system depicted Figure 2-5 is shown:

$$\boldsymbol{M} = \begin{bmatrix} m_{11}+\psi & m_{12} & m_{13} & & m_{1j} \\ m_{21} & m_{22}+\psi & m_{23} & \cdots & m_{2j} \\ m_{31} & m_{32} & m_{33} & & m_{3j} \\ & \vdots & & \ddots & \vdots \\ m_{i1} & m_{i2} & m_{i3} & \cdots & m_{ij} \end{bmatrix} \tag{2.9}$$

Where:

ψ	extra mass contribution
i	row number
j	column number

As it can be seen from Eq. (2.9), assuming $\boldsymbol{M}$ is reduced to account for the boundary conditions, a mass perturbation for the translational DOF in node 1 is implemented.

2.3.2 Stiffness Perturbation

To implement a stiffness perturbation in a beam element of the structure, the local stiffness matrix for the element must be adjusted. This can be done by modifying the modulus of elasticity in the local stiffness matrix for the corresponding element. The implementation of a stiffness perturbation in the FEM-program is exemplified in Eq. (2.10):

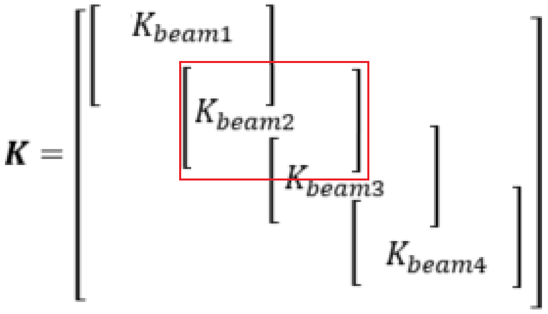

(2.10)

Where:

$\boldsymbol{K}$	global stiffness matrix
$\boldsymbol{K}_{beam,i}$	local stiffness matrix

In this example, a stiffness perturbation is introduced to the second element. The modulus of elasticity for this local stiffness matrix is then modified, by a factor γ, as illustrated in Eq. (2.11):

$$\boldsymbol{K}_{beam2} = \begin{bmatrix} \frac{EA\gamma}{L} & 0 & 0 & -\frac{EA\gamma}{L} & 0 & 0 \\ 0 & \frac{12EI\gamma}{L^3} & \frac{6EI\gamma}{L^2} & 0 & -\frac{12EI\gamma}{L^3} & \frac{6EI\gamma}{L^2} \\ 0 & \frac{6EI\gamma}{L^2} & \frac{4EI\gamma}{L} & 0 & -\frac{6EI\gamma}{L^2} & \frac{2EI\gamma}{L} \\ -\frac{EA\gamma}{L} & 0 & 0 & \frac{EA\gamma}{L} & 0 & 0 \\ 0 & -\frac{12EI\gamma}{L^3} & -\frac{6EI\gamma}{L^2} & 0 & \frac{12EI\gamma}{L^3} & -\frac{6EI\gamma}{L^2} \\ 0 & \frac{6EI\gamma}{L^2} & \frac{2EI\gamma}{L} & 0 & -\frac{6EI\gamma}{L^2} & \frac{4EI\gamma}{L} \end{bmatrix} \tag{2.11}$$

Where:

E	the modulus of elasticity
A	area of cross-section
I	moment of inertia
L	length of element
$\gamma \in [0; 1]$	multiplying constant for stiffness perturbation

2.4 THE SDLID METHOD

The primary idea behind the SDLID method is it operates on the premise of postulated damage patterns, comparing the responses generated by shaped inputs from a reference and a damaged system, as mentioned in Section 1.3. First step in the SDLID scheme is to establish an FE-model of the system being investigated to generate the so-called shaped inputs, which render the perturbation dormant. These inputs are computed using Eq. (2.12):

$$\boldsymbol{u}(s)_i = \boldsymbol{T}_i \boldsymbol{G}_{\bullet,\tau}(s) \boldsymbol{f}_{\tau_i}(s) = \boldsymbol{0} \tag{2.12}$$

Where:

subscript "$\bullet$" denotes all rows

subscript "τ" denotes DOF locations of shaped inputs

$\boldsymbol{T}_i$	interrogation matrix
$\boldsymbol{u}(s)$	complex response
$\boldsymbol{f}_{\tau_i}(s)$	complex shaped inputs

The interrogation matrices, $\boldsymbol{T}_i$, are used in Eq. (2.12) to render the accelerations or strains dormant, depending on what type of damage one interrogates for. The shaped inputs, $\boldsymbol{f}_\tau(s)$, are generated for each interrogation "i", by finding the null space for $\boldsymbol{T}_i \boldsymbol{G}_{\bullet,\tau}(s)$, suppressing certain steady-state vibration quantities. For a harmonic load distribution, the amplitude and phase angle are directly computed as the moduli and arguments of the complex shaped inputs. Reusing the shaped inputs on the damaged structure, leads to responses from the reference and damaged structure, which are calculated in Eq. (2.13) and (2.14):

$$\boldsymbol{X}_u(s) = \boldsymbol{G}_u(s) \boldsymbol{f}_\tau(s) \tag{2.13}$$

$$\boldsymbol{X}_d(s) = \boldsymbol{G}_d(s) \boldsymbol{f}_\tau(s) \tag{2.14}$$

When responses from the reference and damaged system are similar, damage is located, expressed in Eq. (2.15):

$$\boldsymbol{X}_{u,i}(s) = \boldsymbol{X}_{d,i}(s) \tag{2.15}$$

Comparing two responses can be done in several ways, in this thesis the Euclidian distance is used.

$$M_i = \sqrt{\sum (|\boldsymbol{X}_{d,i}(s)| - |\boldsymbol{X}_{u,i}(s)|)^2} \tag{2.16}$$

In practice, the responses from the reference and damaged structure will not be exactly the same, due to noise in the signal and inaccuracies in the FE-model. Hence, the smallest deviation between the responses will indicate the location of the perturbation. If the responses show no clear indication of where the damage is present, engineering judgement will decide if further tests are needed.

Following sections elaborate the construction of the interrogation matrices, $\boldsymbol{T}_i$, for localisation of a mass and stiffness perturbation. Both examples are based on the systems depicted in Figure 2-6 and Figure 2-8.

2.4.1 Interrogation Matrices – Mass Perturbation Localisation

This section describes the interrogation matrices for the system illustrated in Figure 2-6, where a mass perturbation is located at node 3 and shaped inputs placed in node 1, 2 and 4, respectively.

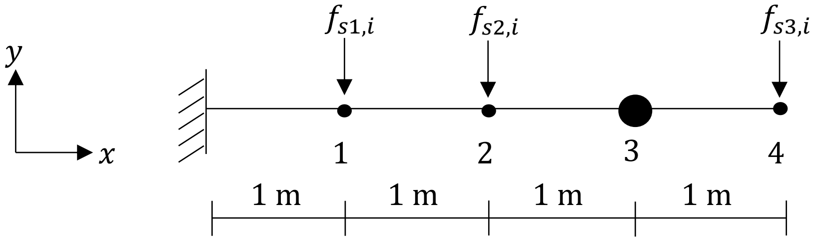

Figure 2-6: Schematic representation of the system for the example case in present section.

To suppress a mass perturbation in a node, the accelerations must be rendered dormant, as illustrated in Eq. (2.1). Since the accelerations are the second derivative of the displacements, suppressing the displacements will also suppress the accelerations. The mass contribution from the rotational DOF is neglected due to the mass perturbation being a point mass.

$$x(t) = 0 \qquad \Rightarrow \qquad \ddot{x}(t) = 0$$

This removes the mass contribution for the specific node. The transfer matrix, $\boldsymbol{G}(s)$, for the system depicted in Figure 2-6 becomes:

$$\boldsymbol{G}(s) = \begin{bmatrix} G_{1,1} & G_{1,2} & \cdots & G_{1,12} \\ G_{2,1} & G_{2,2} & \cdots & G_{2,12} \\ \vdots & \vdots & \ddots & \vdots \\ G_{12,1} & G_{12,2} & \cdots & G_{12,12} \end{bmatrix} \in \mathbb{C}^{n \times n} \tag{2.17}$$

Choosing shaped inputs, "f", and their location, denoted by subscript "τ", the transfer matrix $\boldsymbol{G}(s)$ is for present example reduced to:

$$\boldsymbol{G}_{\bullet,\tau}(s) = \begin{bmatrix} G_{1,2} & G_{1,5} & G_{1,11} \\ G_{2,2} & G_{2,5} & G_{2,11} \\ \vdots & \vdots & \vdots \\ G_{12,2} & G_{12,5} & G_{12,11} \end{bmatrix} \in \mathbb{C}^{n \times p} \tag{2.18}$$

It is important to notice that the number of shaped inputs (p) must be larger than the number of perturbated DOF (q) being investigated for, $(p > q)$, to ensure rank deficiency and that a null space exists.

The interrogation matrices, $\boldsymbol{T}_i$, are used to render each set of DOF being investigated dormant. It is noticed that due to the mass perturbation being a point mass, the matrices only have two rows, extracting the translational DOF from the transfer matrix.

$$\boldsymbol{T}_1 = \begin{bmatrix} 1 & 0 & 0 & 0 & 0 & 0 & \cdots & 0 \\ 0 & 1 & 0 & 0 & 0 & 0 & \cdots & 0 \end{bmatrix} \qquad \in \mathbb{R}^{q \times n}$$

$$\boldsymbol{T}_2 = \begin{bmatrix} 0 & 0 & 0 & 1 & 0 & 0 & \cdots & 0 \\ 0 & 0 & 0 & 0 & 1 & 0 & \cdots & 0 \end{bmatrix} \qquad \text{etc., up to } \boldsymbol{T}_n$$

Hereby, taking the null space for $\boldsymbol{T}_i\boldsymbol{G}_{\bullet,\tau}\,(s)$ for each interrogation, sets of shaped inputs are created corresponding to the number of nodes being rendered dormant. Damage is localised when the vibration signature from the damaged state, generated by the shaped inputs, corresponds with the vibration signature from the reference state, using Eq. (2.16). Figure 2-7 shows a damage pattern plot of the compared responses for the system depicted in Figure 2-6, where the value of M is normalised with respect to the maximum M value.

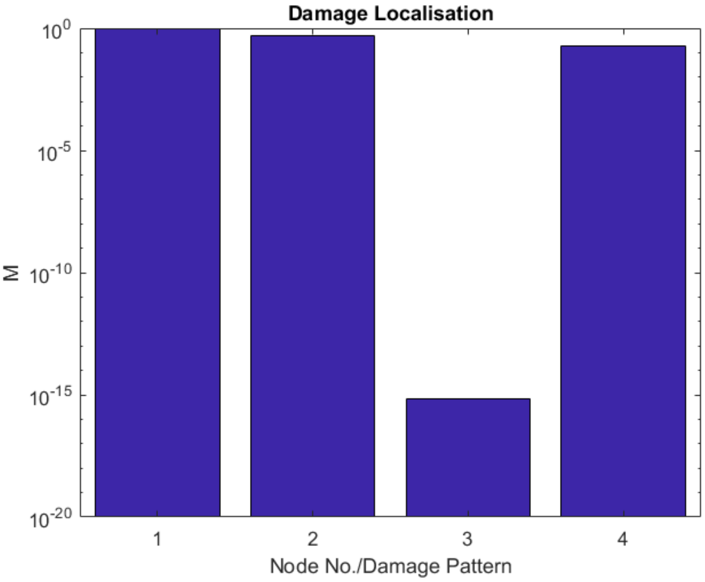

Figure 2-7: Damage pattern plot of mass perturbation example.

As it can be seen from Figure 2-7, the mass perturbation is located at node 3, since the responses between the reference and perturbated systems has the lowest deviation.

2.4.2 Interrogation Matrices – Stiffness Perturbation Localisation

The difference between localising a mass and stiffness perturbation is the construction of the interrogation matrices, $\boldsymbol{T}_i$. As explained in Section 2.4.1, to render the mass perturbation dormant the interrogation matrix suppresses the translational DOF removing the mass contribution for each node respectively. To remove the stiffness contribution from an element, we look at the strain energy for the system, given the structural domain $\Omega = \Omega_H \cup \Omega_D$, where Ω_H and Ω_D are the healthy and damaged subdomain [10]:

$$U_\Omega = \frac{1}{2}\int_\Omega \boldsymbol{\epsilon}^T \boldsymbol{E}\boldsymbol{\epsilon}\, dV \tag{2.19}$$

Where:

$\boldsymbol{\epsilon}$	strain vector	$\in \mathbb{R}^{n\times 1}$
$\boldsymbol{E}$	constitutive matrix	$\in \mathbb{R}^{n\times n}$

Introducing a stiffness perturbation to the system we get following expression:

$$\tilde{U}_\Omega = \frac{1}{2}\int_{\Omega_H} \tilde{\boldsymbol{\epsilon}}^T \boldsymbol{E}\tilde{\boldsymbol{\epsilon}}\, dV + \frac{1}{2}\int_{\Omega_D} \tilde{\boldsymbol{\epsilon}}^T \tilde{\boldsymbol{E}}\tilde{\boldsymbol{\epsilon}}\, dV \tag{2.20}$$

Where:

$\tilde{\boldsymbol{\epsilon}}$	strain vector for perturbated system
$\widetilde{\boldsymbol{E}}$	constitutive matrix for perturbated system

To obtain the same strain energy from the reference and damaged system, then $\widetilde{U}_\Omega = U_\Omega$ and $\tilde{\boldsymbol{\epsilon}} = \boldsymbol{\epsilon}$ must be true. With this knowledge, following expression can be written:

$$\frac{1}{2}\int_{\Omega_H} \boldsymbol{\epsilon}^T \boldsymbol{E}\boldsymbol{\epsilon}\, dV + \frac{1}{2}\int_{\Omega_D} \boldsymbol{\epsilon}^T \widetilde{\boldsymbol{E}}\boldsymbol{\epsilon}\, dV = \frac{1}{2}\int_{\Omega_H} \boldsymbol{\epsilon}^T \boldsymbol{E}\boldsymbol{\epsilon}\, dV + \frac{1}{2}\int_{\Omega_D} \boldsymbol{\epsilon}^T \boldsymbol{E}\boldsymbol{\epsilon}\, dV$$

This can be reduced to:

$$\frac{1}{2}\int_{\Omega_D} \boldsymbol{\epsilon}^T \widetilde{\boldsymbol{E}}\boldsymbol{\epsilon}\, dV = \frac{1}{2}\int_{\Omega_D} \boldsymbol{\epsilon}^T \boldsymbol{E}\boldsymbol{\epsilon}\, dV \tag{2.21}$$

and since $\boldsymbol{E} \neq \widetilde{\boldsymbol{E}}$ then $\boldsymbol{\epsilon} = 0$ in Ω_D.

Eq. (2.21) shows that the interrogation matrices must suppress the strains for an element to render the stiffness perturbation dormant. To do this, the strain interpolation matrix is used:

$$\boldsymbol{\epsilon} = \boldsymbol{B}\boldsymbol{x} \tag{2.22}$$

Where:

$\boldsymbol{B}$	strain interpolation matrix	$\in \mathbb{R}^{q\times n}$
$\boldsymbol{x}$	displacement vector	$\in \mathbb{R}^{n\times 1}$

As shown in Eq. (2.22) the strain interpolation matrix gives a linear relation between the displacements and strains. Using this linear relationship, the interrogation matrices can be constructed to render the stiffness contribution dormant for each element. The strain interpolation matrix for a single beam element from the system depicted in Figure 2-8 is given in Eq. (2.23):

$$\boldsymbol{B} = \begin{bmatrix} -\frac{1}{L} & 0 & 0 & \frac{1}{L} & 0 & 0 \\ 0 & -\frac{6}{L^2} + \frac{12x}{L^3} & \frac{6x}{L^2} - \frac{4}{L} & 0 & \frac{6}{L^2} - \frac{12x}{L^3} & -\frac{2}{L} + \frac{6x}{L^2} \end{bmatrix} \tag{2.23}$$

Where:

x	location along the element

Letting $x = 0$ and $x = L$ yields the strain in each node of the element, respectively. This results in two solutions giving us following interrogation matrix:

$$\boldsymbol{T}_1 = \begin{bmatrix} -1 & 0 & 0 & 1 & 0 & 0 & \cdots & 0 \\ 0 & -\frac{6}{L^2} & -\frac{4}{L} & 0 & \frac{6}{L^2} & -\frac{2}{L} & \cdots & 0 \\ 0 & \frac{6}{L^2} & \frac{2}{L} & 0 & -\frac{6}{L^2} & \frac{4}{L} & \cdots & 0 \end{bmatrix} \in \mathbb{R}^{q \times n} \quad (2.24)$$

The values inside the matrices shift regarding which element's strains must be suppressed. For stiffness perturbation localisation the interrogation matrices from Eq. (2.24) is implemented in Eq. (2.12). Accounting for the orientation of each element we get following expression:

$$\boldsymbol{T}_1 = \begin{bmatrix} -\cos(\theta) & -\sin(\theta) & 0 & \cos(\theta) & \sin(\theta) & 0 & \cdots & 0 \\ \frac{6}{L^2}\sin(\theta) & -\frac{6}{L^2}\cos(\theta) & -\frac{4}{L} & -\frac{6}{L^2}\sin(\theta) & \frac{6}{L^2}\cos(\theta) & -\frac{2}{L} & \cdots & 0 \\ -\frac{6}{L^2}\sin(\theta) & \frac{6}{L^2}\cos(\theta) & \frac{2}{L} & \frac{6}{L^2}\sin(\theta) & -\frac{6}{L^2}\cos(\theta) & \frac{4}{L} & \cdots & 0 \end{bmatrix} \quad (2.25)$$

Using Eq. (2.12), replacing T_1 with Eq. (2.25), the different shaped inputs are computed for stiffness perturbation localisation. Notice, the required shaped inputs needed are $p > 3$ ensuring rank deficiency. A similar example as in previous section is used for numerical validation of stiffness perturbation localisation.

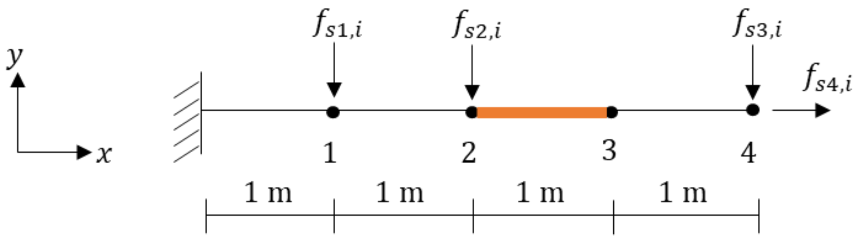

Figure 2-8: Schematic representation of the example with a stiffness perturbation introduced in element 3.

Figure 2-9 shows a damage pattern plot of the system in Figure 2-8 by use of Eq. (2.16).

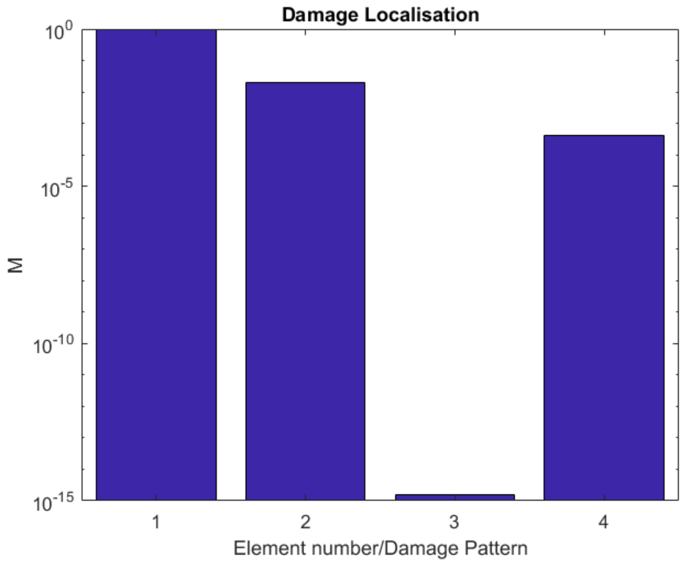

Figure 2-9: Damage pattern plot of SDLID responses.

As Figure 2-9 indicates, the perturbation is located in element 3.

2.4.3 Numerical Simulation

The analytical approach in Section 2.4.1 and 2.4.2 validated the SDLID method theoretically. To simulate a real-life scenario, where white Gaussian noise is introduced, numerical time integration is implemented where extraction of vertical displacements for each node are used for damage localisation.

Mass and Stiffness Perturbation Localisation

Numerical simulation is performed on the same example as presented in Section 2.4.1 and 2.4.2, using the amplitude and phase angle by taking the moduli and argument from the computed shaped inputs used in pervious examples. The timestep used is 0.01s and the total simulation time is 120s to ensure that the transient part is damped out.

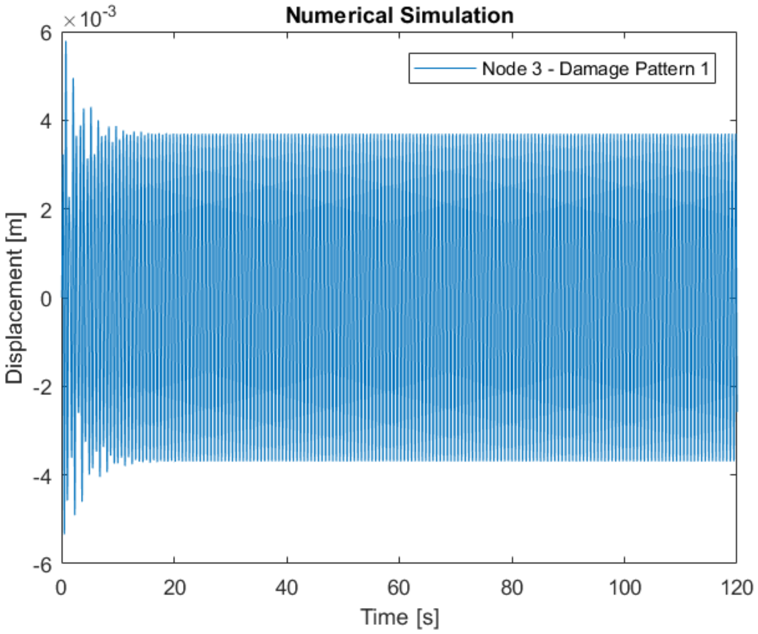

Figure 2-10: Vertical displacement for node 3 from numerical simulation.

As illustrated in Figure 2-10 the transient part is present to approximately 20s. To ensure only steady-state vibration is present, data from 105-120s are used when comparing the healthy and perturbated response for damage localisation.

Figure 2-11a shows clearly how the implemented mass perturbation affects the dynamic behaviour of the system depicted in Figure 2-6. Figure 2-11b shows how damage pattern 3 renders node 3 dormant.

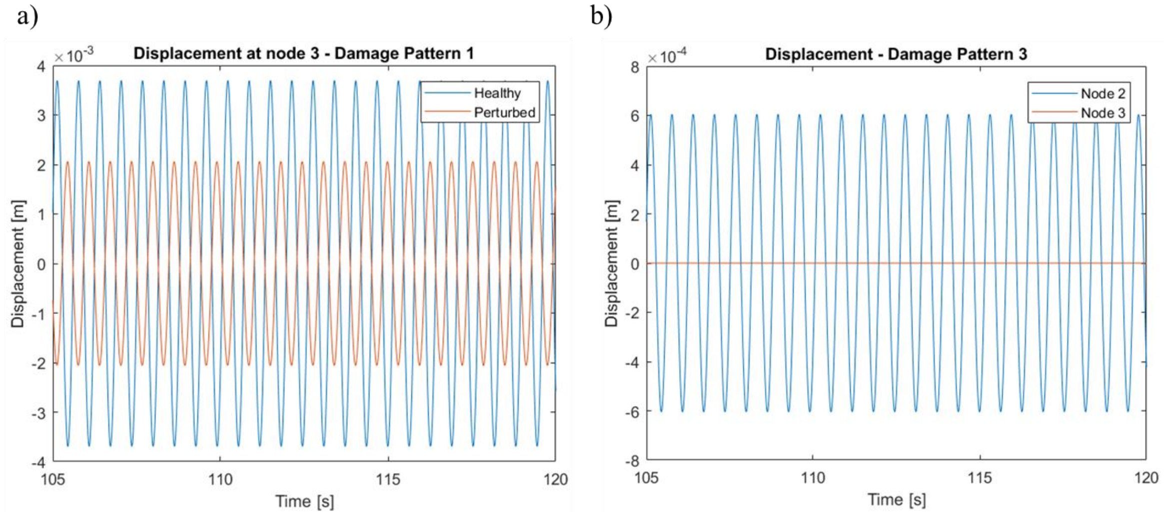

Figure 2-11: Numerical simulation. a) Vertical displacement for healthy and perturbed example. b) Vertical displacement for healthy example.

In Section 2.4, the complex responses are compared by taking the Euclidean distance, but since the responses from the numerical simulations are represented in the time domain we look at the shift in energy from the reference and perturbated response. A further elaboration can be found in Chapter 5. Since the responses illustrated in Figure 2-10 and Figure 2-11 are made under ideal conditions, white Gaussian noise with a signal to noise ratio of 60dB is implemented to simulate real-life measurement.

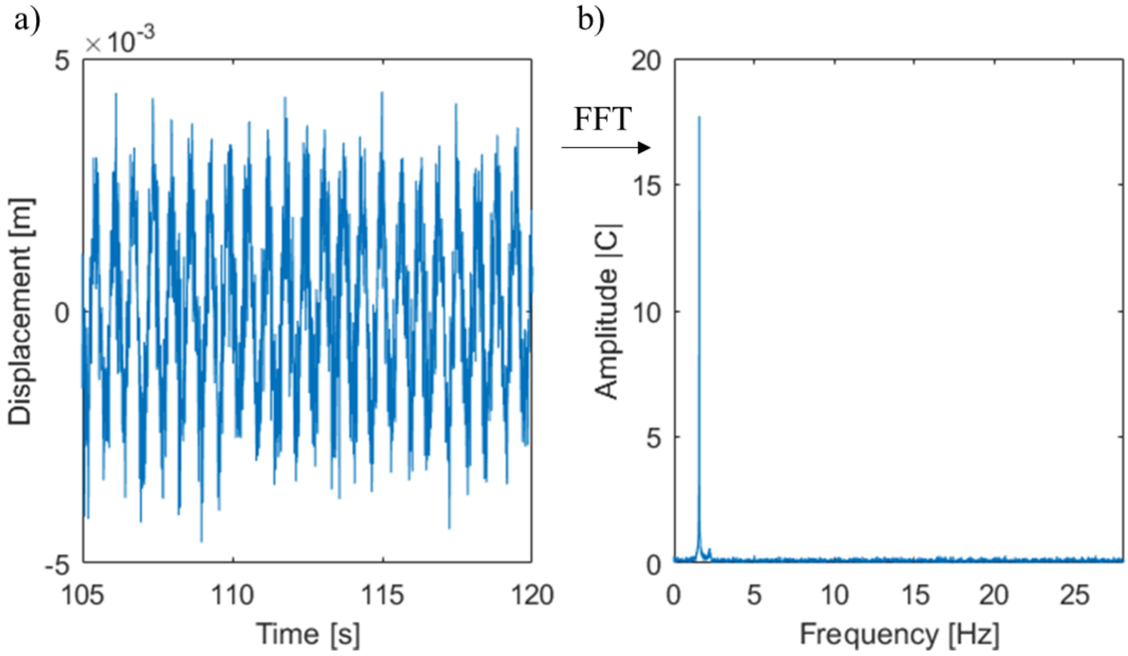

Figure 2-12: Numerical simulation. a) Perturbed response with white Gaussian noise for node 3 from damage pattern 1. b) FFT plot of perturbed response.

Using Eq. (5.3), comparing the peak amplitudes for each damage pattern response allow us to analyse the energy shift between the healthy and perturbated system.

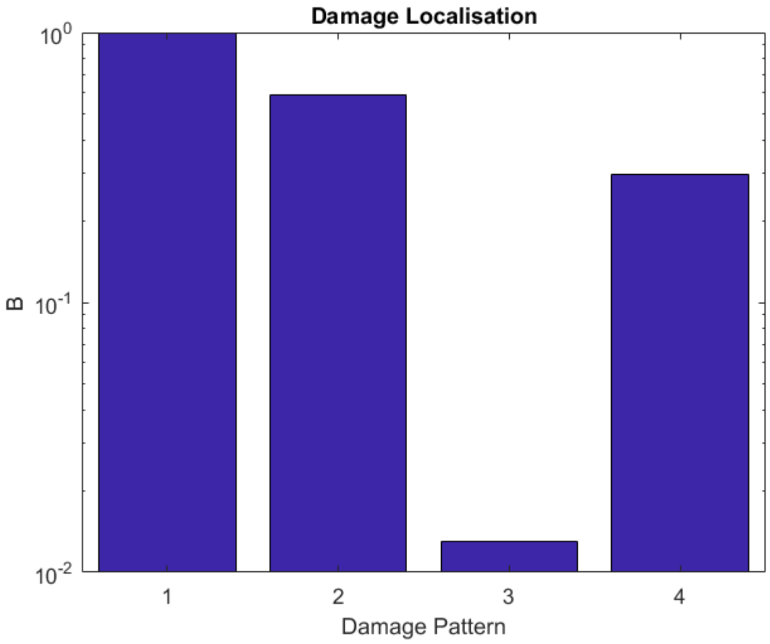

Figure 2-13: Damage pattern plot from numerical simulation of the system depicted Figure 2-6.

As it can be seen from Figure 2-13 the SDLID method is able to localise the mass perturbation in node 3 with white Gaussian noise introduced. To construct a numerical simulation for localisation of a stiffness perturbation same procedure is used.

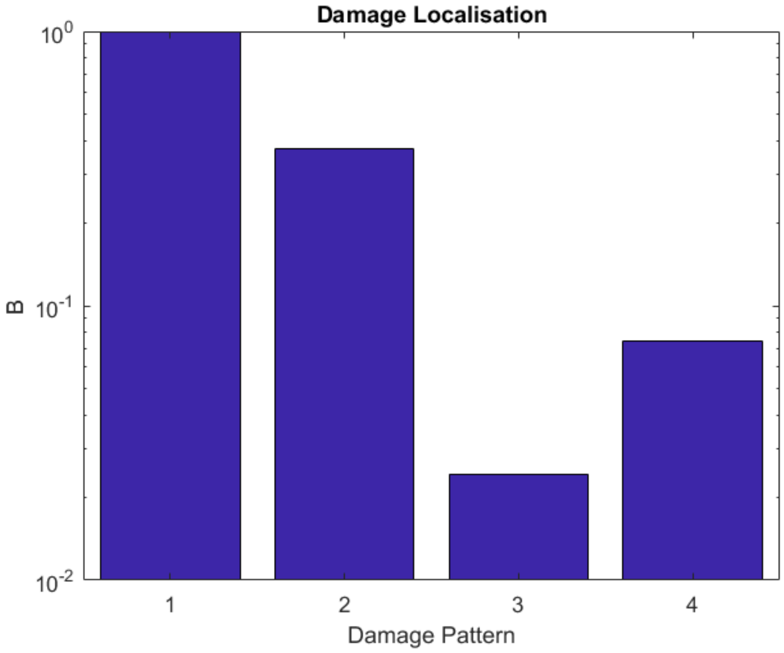

Figure 2-14: Damage pattern plot from numerical simulation of the system depicted in Figure 2-8.

As illustrated in Figure 2-14 damage localisation of the implemented stiffness perturbation in element no. 3 is successful.

2.5 FLOW DIAGRAM OF THE SDLID METHOD

To provide a better understanding of the SDLID approach a flow diagram is constructed which contains the steps for damage localisation, see Figure 2-15.

1) Establish FEM model of reference structure

- Thereby establishing M, C *and* K matrices $M, C, K \in \mathbb{R}^{n\times n}$

2) Transform into complex domain

- Use Laplace transformation to establish transfer matrix $G(s)$ $G(s) \in \mathbb{C}^{n\times n}$

3) Define location (DOF) of shaped inputs p_i

- Location of p_i is indexed by τ_i $p > q \quad where:\ q = suppressed\ DOF$

4) Establish $G_{\bullet}, \tau$(s)

- Consists of all p indexed colums from $G(s)$ $G_{\bullet,\tau} \in \mathbb{C}^{n\times p}$

5) Establish n number of interrogation matrices T_i

- Used in step 6 to interrogate one node or element at the time $T \in \mathbb{R}^{q\times n}$

6) Define shaped inputs - $f_\tau(s)$ - rendering each node domant

- Find null-spaces for $f_\tau(s)$ by Eq.: $TG_{\bullet}, \tau(s) f_\tau(s) = 0$ $f_\tau(s) \in \mathbb{C}^{p\times(p-q)}$

7) Find responses - $X(s)$ - from shape inputs applied to the reference structure

- X(s) = $G_{\bullet}, \tau(s) f_\tau(s)$ $X_u(s) \in \mathbb{C}^{n\times(p-q)}$

8) Establish response of damaged structure from shaped inputs

- Repeat step 7 for the damaged structure.

9) Compare responses from reference and damaged structure

- Damage is located where response from reference and damaged structure are similar

Figure 2-15: Flow diagram for localisation of damage using SDLID.

2.6 SUMMARY

Chapter 2 presents a general introduction to linear vibration theory and modal analysis, which are used for investigating the dynamic behaviour of the frame structure, depicted in Figure 3-1a, and the numerical model. A formulation of the SDLID scheme in the Laplace domain is introduced to ease the computation of the shaped inputs used for the numerical and experimental analyses. Furthermore, numerical implementation of a mass and stiffness perturbation into an FE-model is performed to validate the SDLID method.

3 EXPERIMENTAL WORK

The SDLID method's capabilities of localising damages have, so far, been validated theoretically in articles and present thesis [10]. To validate the SDLID method's capabilities of localising damages in practice, experimental tests are conducted.

To conduct reliable experimental tests for validation of the SDLID method, minimising uncontrolled external influences is desired, hence following are sought:

- A stable test environment
- A structure easy to assemble and dissemble
- High precision excitation and measurement equipment

The following sections elaborate the solutions chosen for fulfilling the mentioned objectives.

3.1 TEST ENVIRONMENT

The Mechanical Laboratory at Aalborg University Esbjerg is chosen as test environment since it provides a controlled environment with regard to temperature, wind and other external influences.

3.2 TEST STRUCTURE

The frame structure used for the experimental work is depicted in Figure 3-1a. The diagonal braces restrict movement into the in-plane axis, indicated by the green arrows in Figure 3-1a. To ease the assemble/disassemble process of the frame structure, welded connections are not considered. Separable homogenous connections, in combination with well-defined elements, are sought.

It is chosen to assemble the frame structure using MakerBeam's aluminium beam elements, due to their simplicity, versatility and low cost. Separable homogeneous connections are obtained with corner cubes, screws and threaded rods, as illustrated in Figure 3-1b, with the individual parts depicted in Figure 3-2. All components are from MakerBeam [11], except the treaded rods which are made in the laboratory.

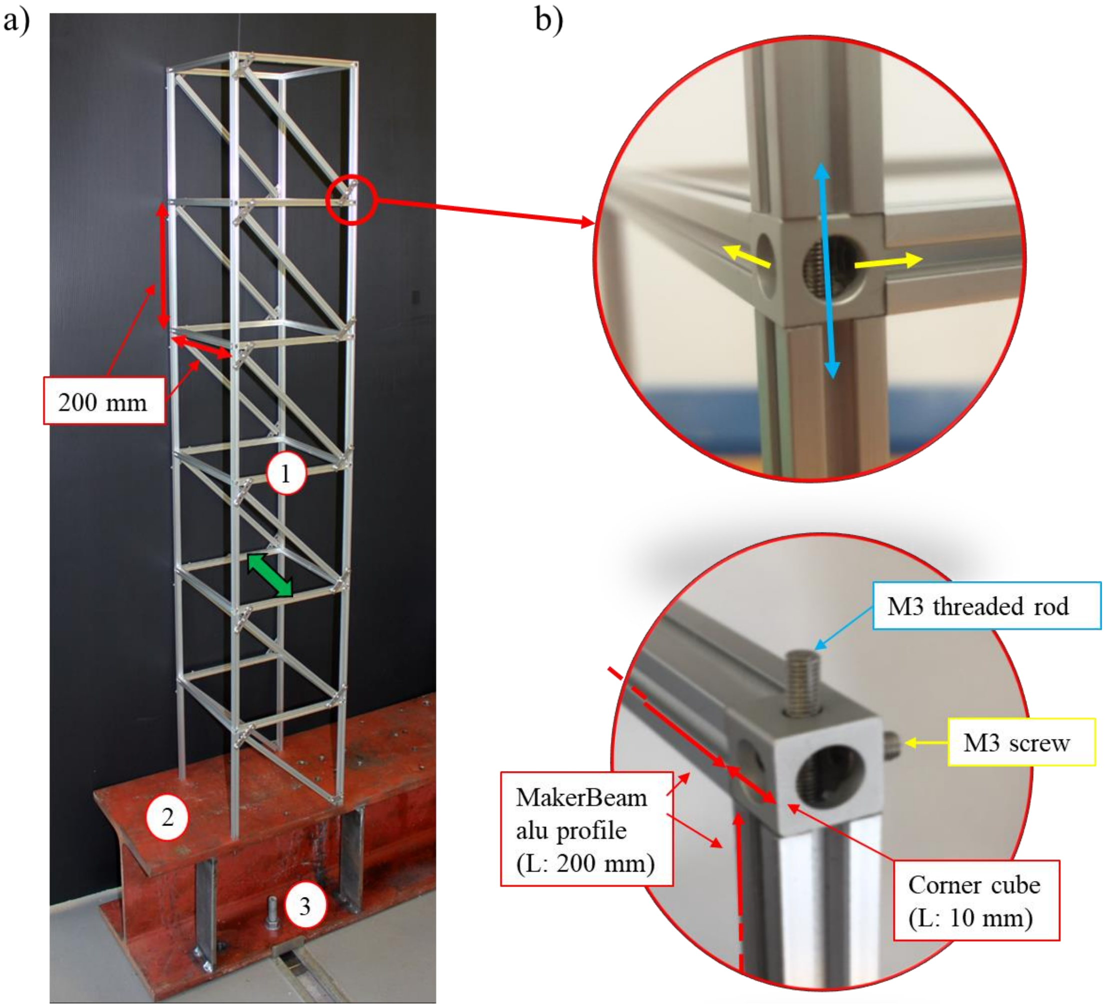

Figure 3-1 a) Frame structure including fixation on I-profile as boundary condition.
Green arrow indicating in-plane excitation, applied on the 2nd floor.
1) Frame structure. 2) I-profile connecting frame structure to laboratory floor, shown in Figure 3-3.
3) Fixation to laboratory floor.
b) Magnified illustrations of 4-way connection between profiles.
Blue arrow illustrates threaded rod connecting MakerBeams through corner cube.
Yellow arrows illustrate screws connecting beams to corner cube. Brace connections are not magnified.

.

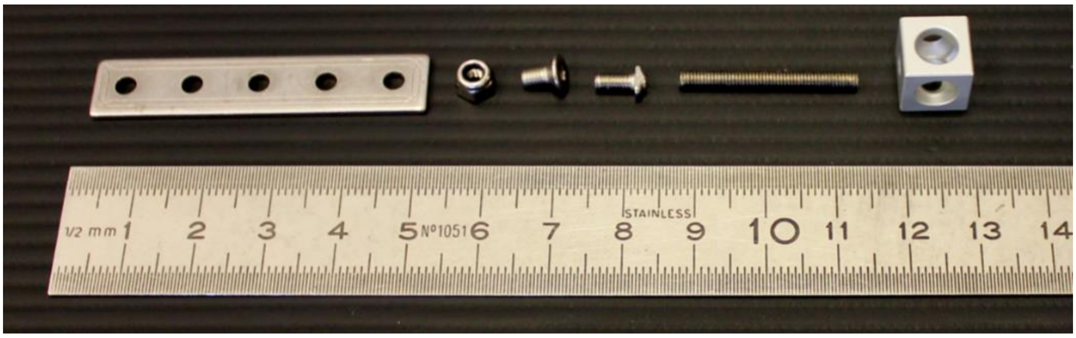

Figure 3-2: Different components used in the structure. From left to right: Straight bracket, self-locking nut, cube-screw, wing-type-bolt, threaded rod and corner cube.

Furthermore, the different elements are reusable for other structure configurations and future projects. Properties of the MakerBeam beam elements are presented in Table 3.1.

Table 3.1: MakerBeam element properties.

Parameter	Symbol	Value	Unit
Cross sectional area	A	$49.091\cdot10^{-6}$	[m^2]
Density	ρ	2900	[kg/m^3]
Modulus of elasticity	E	$68.9\cdot10^{9}$	[Pa]
Poisson ratio	ν	0.33	[-]
Shear modulus	G	$25.9\cdot10^{9}$	[Pa]
Second moment of inertia	Iy & Iz	$495.6\cdot10^{-12}$	[m^4]
Polar moment of inertia	I_x	$991\cdot10^{-12}$	[m^4]

The measured masses of the individual parts and total mass of the assembled structure are presented in Table 3.2.

Table 3.2: Measured masses of individual parts and assembled structure.

Part	[-10^3 kg/pcs]	No. in structure	[-10^3 kg]
MakerBeam profile (200x10x10 mm)	25.0	48	1200
MakerBeam profile (diagonal brace)	33.8	12	405
Corner cube (10x10x10 mm)	1.30	24	31
Screw (corner cube)	0.39	52	20
Threaded rod (corner cube)	1.05	20	21
Straight bracket	6.00	24	144
Self-locking nut (bracket)	0.42	70	29
Wing type bolt (bracket)	0.34	70	24
Sensors	4.8	9	43
Total mass			1918

To minimise the transmission of vibration from the frame structure to the surroundings, the boundary conditions must be fixed. Bolting the structure directly into the laboratory floor requires drilling into the floor, which is not an option. A rigid connection between the rails in the laboratory floor and frame structure is found via a HEB260 profile. Due to practicalities, regarding floor railings, limited space and concurrent experiments in the laboratory, the excitation must be in the HEB260 profile’s weak axis, as seen in Figure 3-1. To conclude how much the flexibility from the I-profile will influence the eigenfrequencies, a study of a simplification of the frame structure into a beam is performed.

Simulating Fixed Boundary Conditions

To ensure that the assumption of a fixed boundary condition in the FE-model is appropriate, rough pre-calculations of the flexibility contribution from the I-profiles weak axis is performed with a simplification of the frame structure into a beam element. The calculations indicate that the flexibility contribution from the weak axis of the HEB profile will affect the eigenfrequencies of the simplified structure as seen in Table 3.3

Table 3.3: Deviation of the first three in-plane eigenfrequencies regarding flexibility contribution from I-profile.

Eigenmode	Difference in eigenfrequency [%]
1	0.059
2	0.104
3	0.159

Though the difference in eigenfrequencies in Table 3.3 is relatively small, two reinforcement plates are welded on each side of the profile, as shown in Figure 3-3, to minimise the deviations even further. Steel shims are positioned between floor and HEB260 to level the boundary conditions for the frame structure, as shown in Figure 3-3.

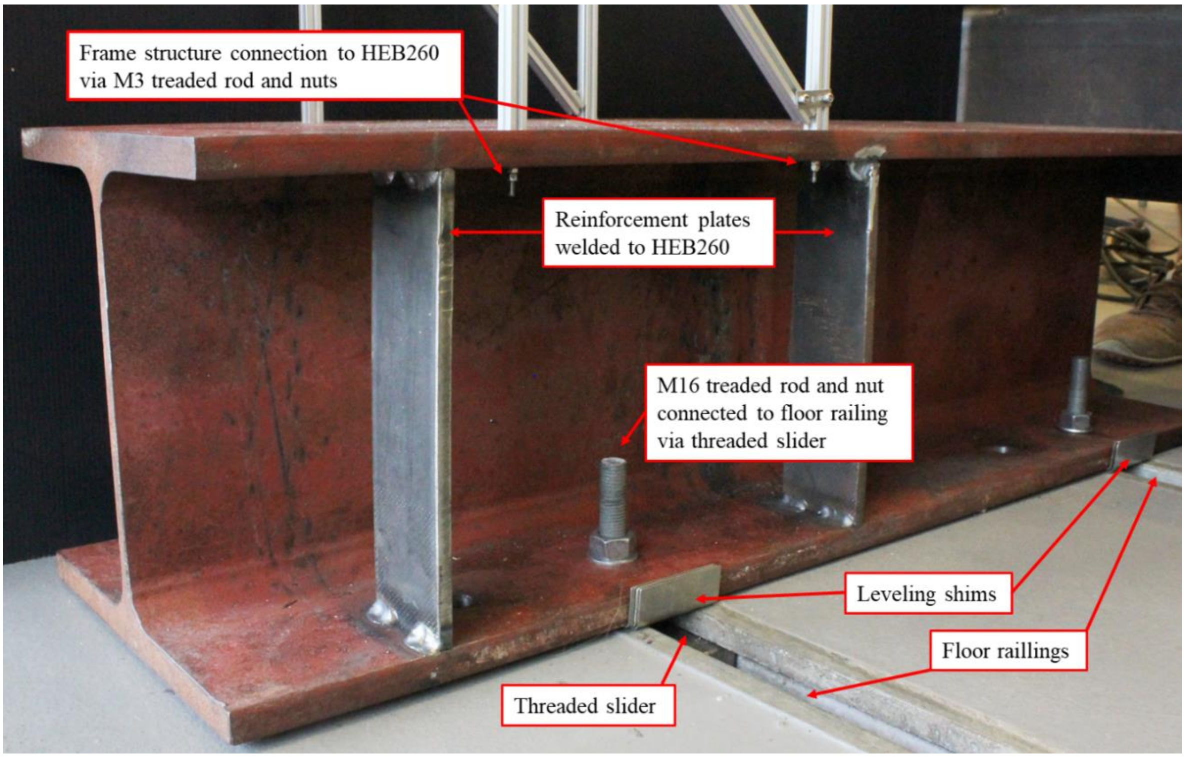

Figure 3-3: Practical accomplishment of relative rigid boundary condition.

After assembling the frame structure, connecting it to the HEB260 and fixating it to the laboratory floor, an experimental stiffness test is performed as illustrated in Figure 3-4.

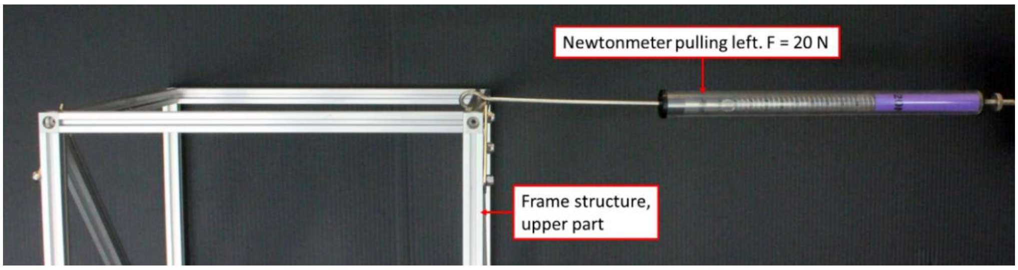

Figure 3-4: Experimental stiffness test performed at the top of the frame structure.

The test is performed by applying different horizontal forces at the top point centre of the frame structure’s weak axis and measuring each displacement. The averaged result in weak axis displacement is shown in Table 3.4.

Table 3.4: Displacement of frame structure.

Assembled frame structure properties - experimental & FEM	
Displacement, weak axis, $F_{horisontal} = 20\text{N}$ Experimental	$4.50\cdot10^{-3}$ [m]
Displacement, weak axis, $F_{horisontal} = 20\text{N}$ FEM (before tuning)	$1.87\cdot10^{-3}$ [m]

Table 3.4. displays the difference between displacement in the FE-model and the frame structure. The extra flexibility in the frame structure is assumed to be caused by lower stiffness in connections, which will be addressed in Chapter 4.

3.3 TEST EQUIPMENT

The measurement and excitation equipment from Brüel & Kjær used for the experimental work are depicted in Figure 3-5 with selected configurations stated in Table 3.5 - Table 3.7. The initial test setup includes one actuator and nine accelerometers, and their respective locations are seen in Figure 3-5. The cabling connected to the accelerometers were lead upwards on to an aluminium beam, depicted in Figure 3-6, to reduce the influence from gravity and damping.

Harmonic Excitation

The excitation mechanism, which is depicted part by part in Figure 3-5c, transfers and measures force from an actuator to the frame structure. The path of this is described below with reference to Figure 3-5c: The actuator is attached to a sturdy steel column via brackets (1) providing a steady ground. The actuator (2) produces vibrations that are transferred via the stinger (3), to the force transducer (4) which measures the input to the structure.

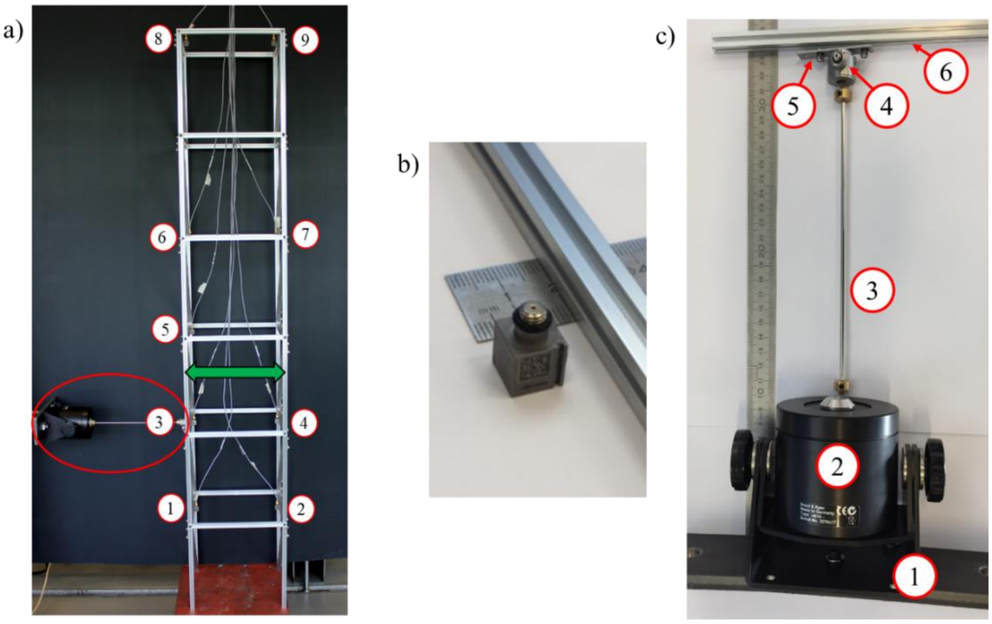

Figure 3-5: Excitation and measurement equipment.
a) Red circle: placement of actuator on 2nd floor. Red number: distribution of accelerometers.
b) Accelerometer and section of MakerBeam beam
c) 1) Brackets connecting actuator to steady column. 2) Actuator. 3) Stinger. 4) Force transducer.
5) Force transducer and MakerBeam beam. 6) Section of MakerBeam beam.

.

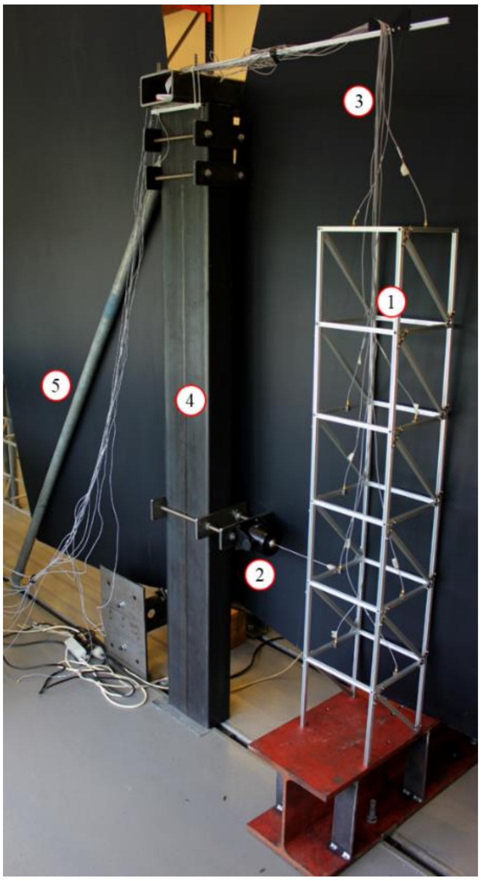

Figure 3-6: Test setup with steel column and reinforcement brace. 1) Frame structure. 2) Actuator.
3) Upwards cabling from accelerometers. 4) Steel column. 5) Reinforcement brace.

The steel column used as boundary condition for the actuator is not sufficiently steady when exciting the frame structure in the interval of approximately 22-37Hz. This was concluded after audio inspection of the steel column, where indication of resonance was present. This lead to reinforcement with a steel brace, as depicted in Figure 3-6, providing extra stiffness and raising the steel columns first eigenfrequency to approximately 80Hz. This is close to the frame structure's third eigenfrequency, which is seen from the disturbances in the third eigenfrequency in Figure 3-9. The test setup is still evaluated as acceptable, since the shaped inputs are to be applied beneath the frame structure's first eigenfrequency.

Selected data for the actuator are seen in Table 3.5 [15].

Table 3.5: Brüel & Kjær, Mini shaker Type 4810 selected data.

Characteristic	Value
Force rating	10 [N]
Frequency range	$< 18 \cdot 10^3$ [Hz]

Harmonic inputs from the actuator are measured by the force transducer, depicted in Figure 3-5c, no. 4. The force transducer measures the compressive and tensile forces uniaxially, at the point right before contact with the structure in question. Meaning that flexibility, and other sources of error, from the stinger and backwards are minimised from the measurements. Selected data for the force transducer are in Table 3.6 [16].

Table 3.6: Selected data for DeltaTron Force Transducer Type 8230-001.

Characteristic	Value
Full scale force range compression	220 [N]
Full scale force tension	220 [N]
Mounted resonance frequency	$75 \cdot 10^3$ [Hz]
Linearity error at full scale	$< \pm 0.01$

Measuring Responses

The response from the frame structure is measured by uniaxial accelerometers depicted in Figure 3-5b with selected configuration in Table 3.7 [17]. The out of plane (OOP) and twisting eigenmodes affect the measured in-plane accelerations, resulting in small peaks in the frequency response function (FRF), as seen in Figure 3-9. Determination of the OOP and twisting eigenfrequencies are performed via impulse excitation equipment and is elaborated in Appendix A.

Table 3.7: Selected data for DeltaTron Accelerometer Type 4507 B.

Characteristic	Value
Frequency range	0.3 to 6000 [Hz]
Mounted resonance frequency	$18 \cdot 10^3$ [Hz]
Transverse sensitivity	< 0.05

The data from each accelerometer is transferred to the acquisition software, where the accelerations are processed, saved or withdrawn for further analysis.

3.4 EXPERIMENTAL MODAL ANALYSES

The FE-model's modal parameters are computed using Eq. (2.2) as elaborated in Chapter 2. To obtain the frame structure's actual modal parameters experimental modal analyses (EMA) are conducted. Present section will discuss how the frame structure's modal parameters are obtained, namely:

- Modal frequencies
- Modal damping ratios
- Mode shapes

Experimental analyses of a structure can be done in several ways. Basically, they consist of excitation of the structure and data acquisition from one or several points at the structure. The type of input could be:

- Harmonic excitation
- Impulse
- Pull-and-release of the structure – decaying free vibration

With acquired input and output data the modal parameters can be estimated by use of the FRF, elaborated in Section 3.4.2. A flow chart of the process for acquiring the modal parameters is illustrated in Figure 3-7.

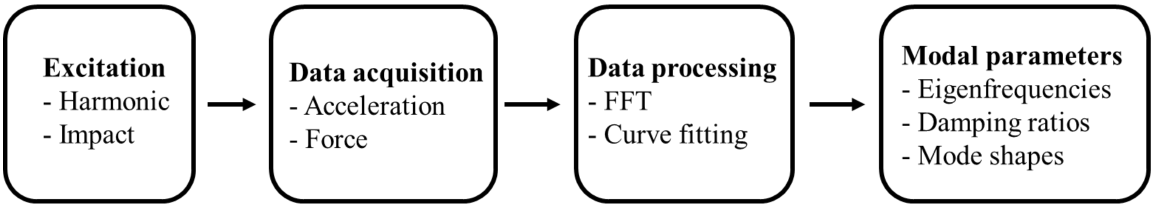

Figure 3-7: Flow chart of working process for acquiring experimental modal parameters.

3.4.1 Experimental Setup

Experimental data for the frame structure is obtained by harmonic and impulse excitation and the respective forces and accelerations are extracted from the data acquisition software PulseReflex. The initial laboratory test setup is depicted in Figure 3-8. It is noticed that the actuator is applying force on the 2nd floor, which is evaluated as suitable for activating the first three in-plane eigenmodes.

It is chosen to place accelerometers in pairs on each floor, giving the possibility of plotting mode shapes for both front and rear side of the frame structure. The data collection equipment available restricts the use of accelerometers to a maximum of nine. Based on visual inspection of the numerical mode shapes, it is evaluated that accelerometers on the 5th floor and rear side of the 3rd floor would contribute the least, hence they are omitted.

Since the loading frequency of the shaped inputs is beneath the first eigenfrequency of the frame structure, see Chapter 5, only the first three in-plane eigenmodes are estimated by conducting sine sweeps.

Figure 3-8: Experimental setup of frame structure.

3.4.2 Sine Sweep Excitation

Performing sine sweeps on the frame structure are done with the setup of harmonic actuator, force transducer and accelerometers as depicted in Figure 3-8. When conducting a sine sweep test, the frequency of the harmonic input is increased stepwise. To ensure consistency ten sine sweeps are conducted and the resulting FRFs are illustrated in Figure 3-9. When the loading frequency is near the structure's eigenfrequencies resonance occurs, making the response oscillate with greater amplitude, which causes the peaks as illustrated in Figure 3-9.

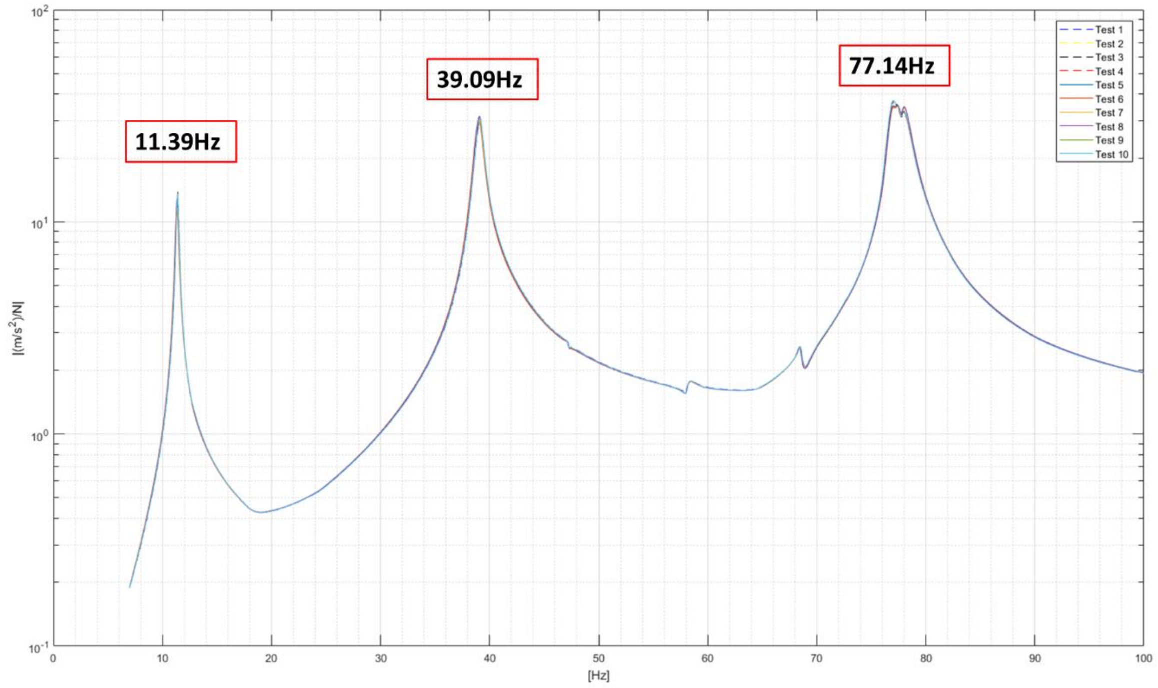

Figure 3-9: Plot of the resulting ten FRFs from the conducted sine sweeps with calculated averaged values for the first three in-plane eigenmodes.

By use of the frequency response function shown in Eq. (3.1), the modal parameters are obtained.

$$\boldsymbol{F}(\omega)\,\boldsymbol{H}(\omega) = \boldsymbol{X}(\omega) \tag{3.1}$$

Where:

$\boldsymbol{H}(\omega)$	frequency response function
$\boldsymbol{X}(\omega)$	complex output
$\boldsymbol{F}(\omega)$	complex input

As seen from Eq. (3.1), the FRF operates as the transfer function depicted in Figure 2-2.

Curve-Fitting – Rational Fractional Polynomial Z-Method

To estimate the modal parameters from the data depicted in Figure 3-9, a curve-fit is implemented. Curve-fitters transform a data set into a mathematical function, enabling estimation of modal parameters from measured data. They can be divided into single-degree-of-freedom (SDOF) and MDOF curve-fitters, where SDOF is used for lightly coupled modes and MDOF for heavily coupled modes [18].

The PulseReflex software contains several curve-fitters of which present thesis uses the rational fractional polynomial z-method [18]. Figure 3-10 shows an FRF from 0 - 400Hz, where the eigenfrequencies of interest are between 7 – 90Hz (yellow area). Extracting modal parameters from the first three eigenmodes is performed by implementing a SDOF curve-fit illustrated in Figure 3-10.

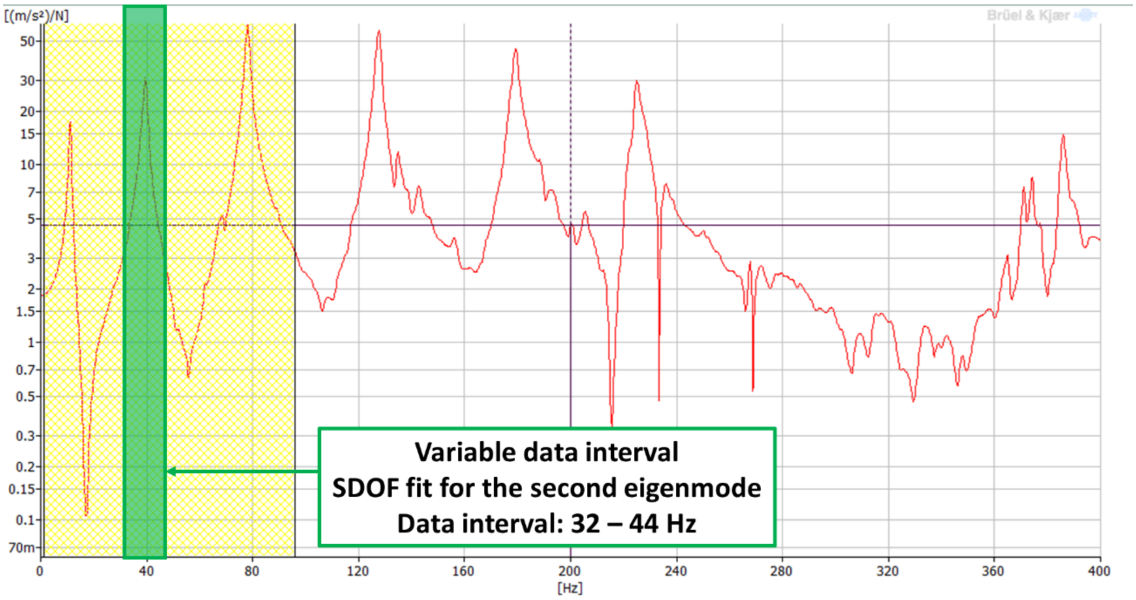

Variable data interval
SDOF fit for the second eigenmode
Data interval: 32 – 44 Hz

Figure 3-10: Curve-fitting in PulseReflex of FRF from conducted sine sweep. Yellow area shows the frequency band of interest where the first three in-plane eigenmodes are located. Green area shows the SDOF curve-fit for approximation of modal parameters for second eigenmode.

Results obtained from the ten sine sweeps are presented in Table 3.8 and averaged values plotted in Figure 3-9.

Table 3.8: Modal parameters acquired from curve-fitting of ten sine sweeps.

Test no	Eigenfrequency [Hz]			Damping ratio [%]		
	1.	2.	3.	1.	2.	3.
1	11.4	39.1	77.1	1.18	1.05	0.960
2	11.4	39.1	77.1	1.10	1.03	1.05
3	11.4	39.1	77.0	1.06	1.03	1.24
4	11.4	39.1	77.0	1.13	1.01	1.03
5	11.4	39.1	77.0	1.11	1.00	1.01
6	11.3	39.0	77.3	1.20	1.02	0.920
7	11.4	39.1	77.4	1.16	1.01	0.610
8	11.4	39.1	77.4	1.09	0.980	1.20
9	11.4	39.1	77.0	1.05	0.970	1.10
10	11.4	39.1	77.0	1.14	0.960	1.06
μ (Mean)	11.4	39.1	77.1	1.12	1.01	1.02
σ (Standard deviation)	0.0316	0.0246	0.175	0.0480	0.0271	0.173

As it can be seen from Table 3.8 the eigenfrequencies and damping ratios from all experiments are relatively consistent. Furthermore, it is noticed that the standard deviations increase at the third eigenmode, indicating less consistency in the data, though still evaluated as sufficiently accurate. Also, we see great uncertainty associated with damping estimates.

3.5 SUMMARY

This chapter gives a description of the EMA conducted on the frame structure to establish the first three in-plane eigenmodes, depicted in Figure 3-9, where the important aspects, such as fixation of the frame structure, are evaluated. Furthermore, the apparatus used for conducting the experimental tests are presented.

The first three in-plane eigenmodes are seen in Figure 3-9, where irregularities in the curves around 57Hz and 69Hz are noticed. The irregularities are caused by a twisting and the first OOP bending mode which are elaborated in Appendix A. Since the in-plane eigenfrequencies obtained from the EMA deviates from the numerical FEM-program, as shown in Table 4.1, tuning of the FE-model is required.

4 DEVELOPMENT OF FE-MODEL

As explained in Chapter 3, the SDLID method is tested on a frame structure which is illustrated in Figure 3-1. To ensure that the computed shaped inputs are designed correctly, the structure's parameters (stiffness and mass) in the FEM-program must resemble the frame structure. This is done by implementing extra mass contributions from the corner connections and accelerometers into the FE-model and reduce joint stiffness.

4.1 INITIAL COMPARISON

To ensure that the FE-model corresponds with the experimental modal parameters, the FE-model's eigenfrequencies are compared with the eigenfrequencies obtained from the EMA, elaborated in Section 3.4.2. It should be noted that comparison of the eigenfrequencies is performed for the first three in-plane eigenmodes.

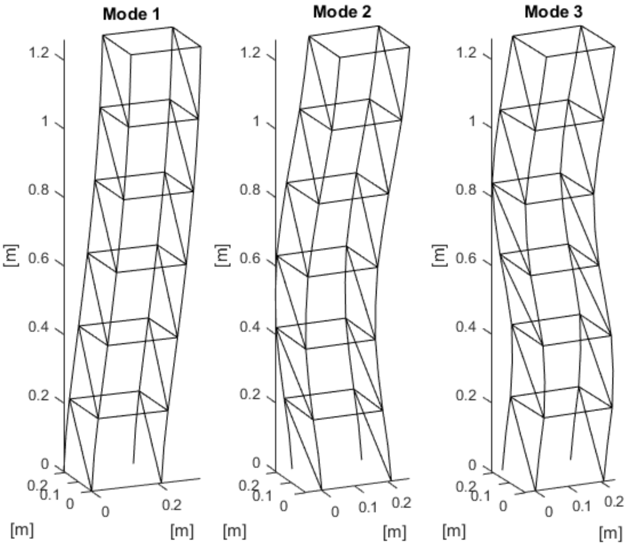

Figure 4-1: Excited in-plane mode shapes from the FEM-program in MATLAB.

Figure 4-1 shows the mode shapes of the first three in-plane eigenmodes used for tuning of the FE-model in accordance to the frame structure.

Table 4.1: Eigenfrequencies from untuned FE-model and experimental modal analysis on frame structure.

Eigenmode	FEM [Hz]	Experiment [Hz]	Deviation [%]
Mode 1	19.6	11.4	71.9
Mode 2	61.9	39.1	58.3
Mode 3	112	77.1	45.3

As Table 4.1 indicates, the eigenfrequencies from the experimental modal analysis are lower than the computed eigenfrequencies in the FEM-program. This indicates that the mass and stiffness for the FE-model do not correspond with the experimental setup in the laboratory. To ensure that the computed shaped inputs will render certain steady-state vibration quantities dormant, the FE-model is tuned regarding the mass and stiffness.

4.2 MASS TUNING

As explained in Section 3.2, the frame structure is constructed using components from MakerBeam. To obtain a reduction in eigenfrequencies of the FE-model the mass contribution from the different components used to assemble the structure, illustrated in Figure 3-2, is implemented in the mass matrix at the translational DOF, corresponding to the location of the corner-connections and accelerometer placement, see Figure 4-2. The mass from the cables and force transducer are neglected, and the mass tuned eigenfrequencies are shown in Table 4.2.

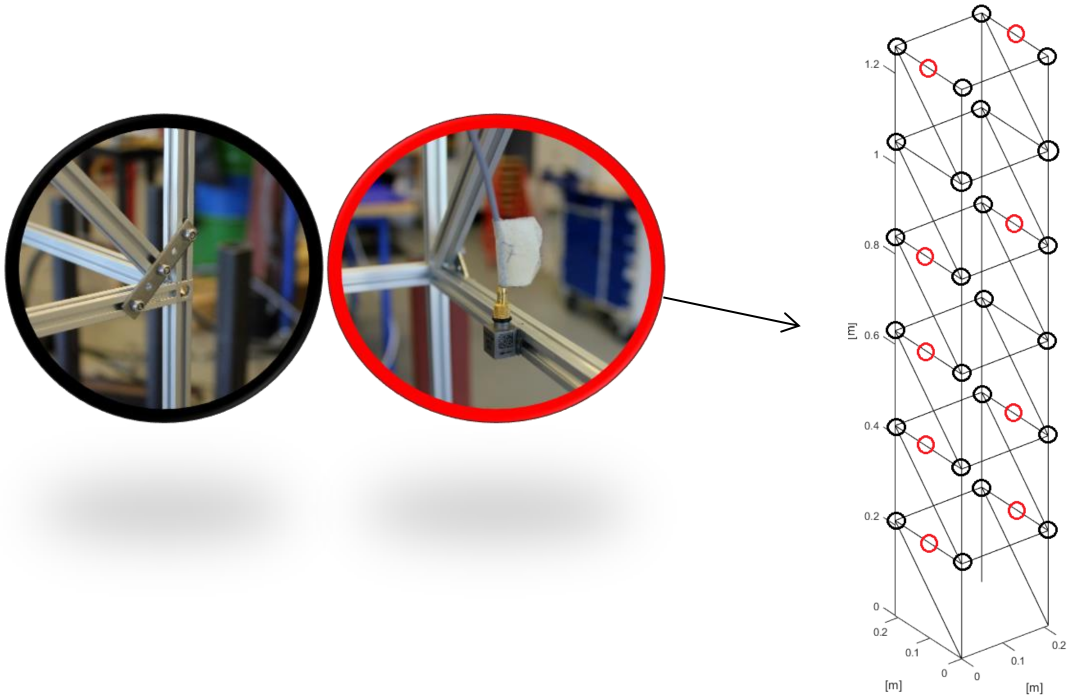

Figure 4-2: Corner-connections (black circle) of the structure and placement of accelerometer (red circle).

Table 4.2: Eigenfrequencies for the FE-model after mass tuning.

Eigenmode	FEM [Hz]	Experiment [Hz]	Deviation [%]
Mode 1	17.5	11.4	53.5
Mode 2	55.2	39.1	41.2
Mode 3	100	77.1	29.7

The mass tuning of the FE-model changed the eigenfrequencies with an average of 41.5% for all eigenmodes. Though the mass tuning lowered the eigenfrequencies of the FE-model, the deviation is still too high.

4.3 STIFFNESS TUNING

The results presented in Table 3.4 and Table 4.2 indicate a demand for reduction in stiffness in the FE-model. A visual inspection of the frame structure is performed to see if any obvious stiffness related deviations are present.

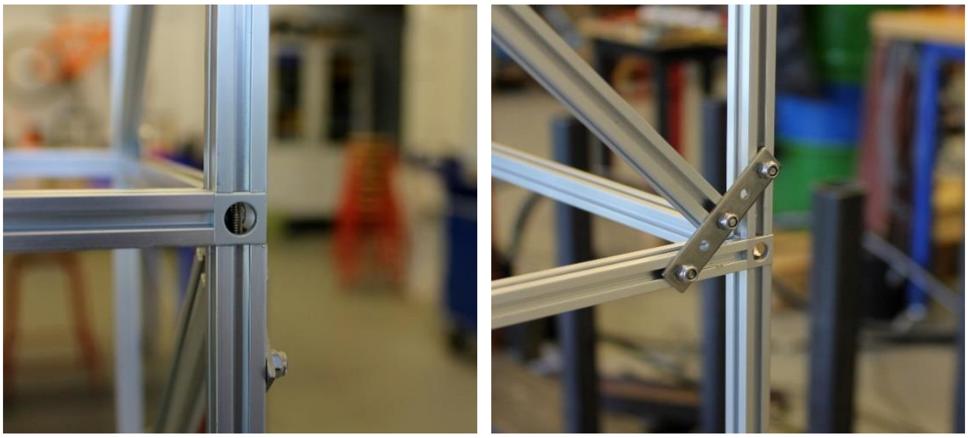

Figure 4-3: Corner connections of frame structure.

It is noticed that the corner-cubes, which connect the beams, are hollow, where in the FE-model the elements are assembled as they were attached to each other (no corner-cube). This indicates that the computed stiffness in the corners for the FE-model is larger than the actual stiffness, which is countered by implementing rotational springs.

4.3.1 Implementation of Rotational Spring

Implementing a rotational spring at each corner of the frame structure allows us to reduce the stiffness from rotation for each corner, hereby reducing the eigenfrequencies of the FE-model. To introduce a rotational spring, a decoupling of the DOF regarding rotation is performed. Implementation of a rotational spring is elaborated below using following example:

Example

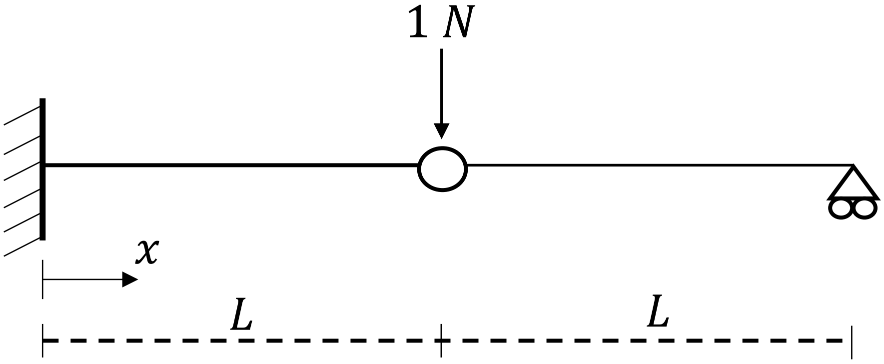

Figure 4-4: Simple example of a beam with a charnier joint.

The example, illustrated in Figure 4-4, is fixed supported on the left side, and simply supported on the right with a charnier located in the middle. To introduce a charnier in the FEM-program, the rotation from the two elements must decouple.

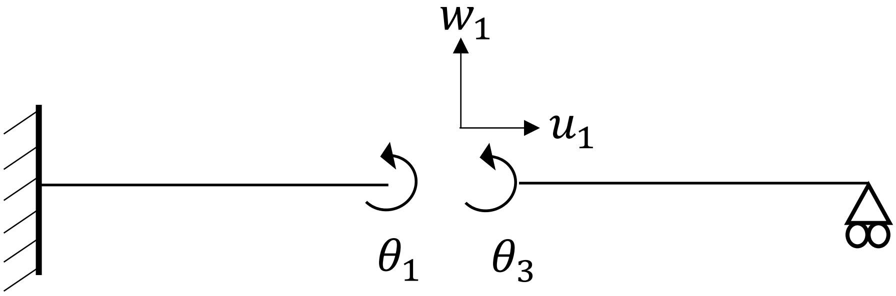

Figure 4-5: Implementation of charnier in the FEM-program.

As shown in Figure 4-5, an additional rotational DOF has been introduced in the charnier-node. Hereby, the rotation from both elements are decoupled, and only the translational DOF in the charnier are shared. The stiffness matrix for the system depicted in Figure 4-5 becomes:

$$\boldsymbol{K} = \begin{array}{c c} & \begin{array}{cccccc} u_1 & w_1 & \theta_1 & u_2 & \theta_2 & \theta_3 \end{array} \\ \begin{array}{c} u_1 \\ w_1 \\ \theta_1 \\ u_2 \\ \theta_2 \\ \theta_3 \end{array} & \begin{bmatrix} k_{1,1} & 0 & 0 & k_{1,4} & 0 & 0 \\ 0 & k_{2,2} & k_{2,3} & 0 & k_{2,5} & k_{2,6} \\ 0 & k_{3,2} & k_{3,3} & 0 & 0 & 0 \\ k_{4,1} & 0 & 0 & k_{4,4} & 0 & 0 \\ 0 & k_{5,2} & 0 & 0 & k_{5,5} & k_{5,6} \\ 0 & k_{6,2} & 0 & 0 & k_{6,5} & k_{6,6} \end{bmatrix} \end{array} \tag{4.1}$$

The additional rotation DOF, θ_3, is placed at the end of the matrix for the corresponding row and column to ease the computations, programming wise. Notice the “zero-locations” in Eq. (4.1) which shows the decoupling between the different DOF. Validating the implementation of rotational spring is performed by comparing vertical displacement at the charnier node in the FEM-program with an analytical calculation for the example shown in Figure 4-5.

$$w_{analytical}(x) = \frac{Px^3}{6EI}(-3L + x) \quad \text{for} \quad 0 \leq x \leq L \tag{4.2}$$

Where:

P	point force
x	defines the location on the beam

The vertical displacement at the charnier-node from Eq. (4.2) and FEM becomes:

$$w_{analytical}(L = 2\,m) = -7.81 \cdot 10^{-2}\text{m}$$

$$w_1 = -7.81 \cdot 10^{-2}\text{m}$$

The results above show a successful implementation of the charnier in the FEM-program, which enables the possibility for implementing a rotational spring. This is done by coupling the two rotations, θ_1 and θ_3, in Eq. (4.1) with a 2 × 2 matrix:

$$\boldsymbol{K}_{spring} = \begin{bmatrix} K_r & -K_r \\ -K_r & K_r \end{bmatrix} \tag{4.3}$$

Where:

$\boldsymbol{K}_{spring}$	stiffness matrix representing the rotational spring
K_r	stiffness contribution from the rotational spring

Eq. (4.3) can then be implemented in Eq. (4.1) to couple θ_1 and θ_3:

$$\boldsymbol{K} = \begin{bmatrix} k_{1,1} & 0 & 0 & k_{1,4} & 0 & 0 \\ 0 & k_{2,2} & k_{2,3} & 0 & k_{2,5} & k_{2,6} \\ 0 & k_{3,2} & k_{3,3}+K_r & 0 & 0 & -K_r \\ k_{4,1} & 0 & 0 & k_{4,4} & 0 & 0 \\ 0 & k_{5,2} & 0 & 0 & k_{5,5} & k_{5,6} \\ 0 & k_{6,2} & -K_r & 0 & k_{6,5} & k_{6,6}+K_r \end{bmatrix} \tag{4.4}$$

In theory, when the value of K_r becomes high enough for the given example, it will simulate a beam without a charnier, coupling the two rotations as illustrated in Figure 4-6.

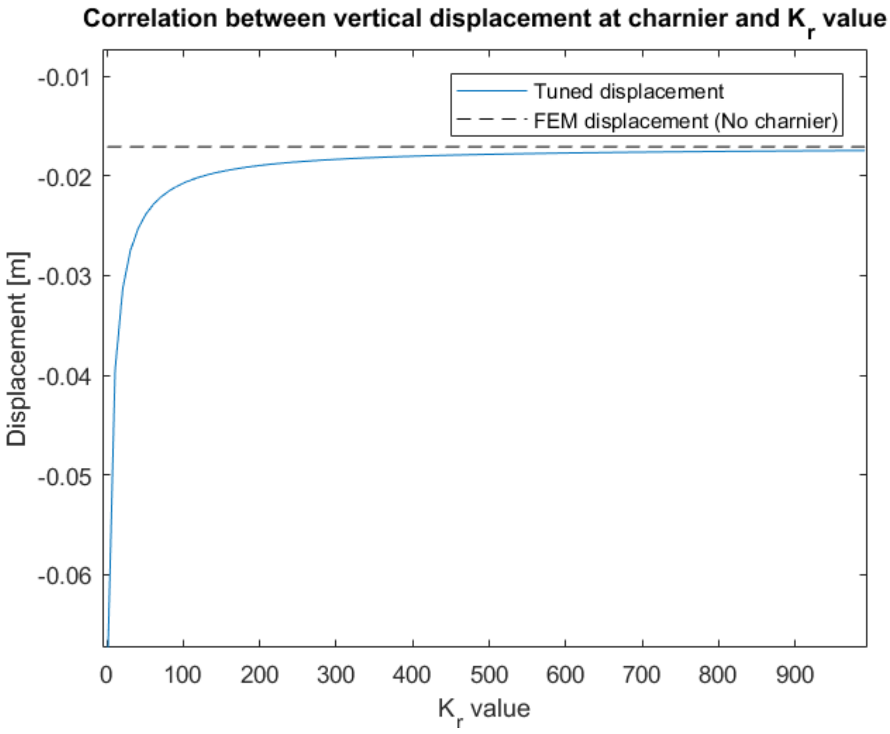

Figure 4-6: Vertical displacement of charnier node from previous example.

Rotational springs are implemented at each corner-cube of the frame structure, where K_r is tuned until the modal parameters of the FE-model correspond to those obtained experimentally.

Table 4.3: Eigenfrequencies from the tuned FE-model, with $\mathrm{K_r} = 400\mathrm{N \cdot m}$, compared with the experimental modal analysis.

Eigenmode	Tuned FE-model [Hz]	Experiment [Hz]	Deviation [%]
Mode 1	11.7	11.4	2.63
Mode 2	39.3	39.1	0.512
Mode 3	77.8	77.1	0.908

As illustrated in Table 4.3, the deviations between the eigenfrequencies from the tuned FE-model and the experimental modal analysis are relatively small. To ensure that the mode shapes between the FE-model and frame structure resemble with one another, the modal assurance criterion (MAC) value is computed.

4.3.2 Modal Assurance Criterion

When tuning the frame structure, it is not sufficient to evaluate the results regarding the eigenfrequencies for validation. The mode shapes must also correspond with each other to ensure the dynamic behaviour for the FE-model resembles the frame structure. The MAC is one of the most popular tools to compare mode shapes. The MAC value is the square of correlation between two modal vectors and is defined as [19]:

$$MAC(r,q) = \frac{\left|\boldsymbol{\phi}_{Ar}^{T}\,\boldsymbol{\phi}_{Bq}^{*}\right|^{2}}{\boldsymbol{\phi}_{Ar}^{T}\,\boldsymbol{\phi}_{Ar}^{*}\,\boldsymbol{\phi}_{Bq}^{T}\,\boldsymbol{\phi}_{Bq}^{*}} \tag{4.5}$$

Where:

r, q	compared eigenmodes
$\boldsymbol{\phi}_A$	experimental modal vector
$\boldsymbol{\phi}_B$	FEM modal vector
$\boldsymbol{\phi}^*$	complex conjugate of ϕ

From Eq. (4.5), the MAC will take a value between 0 and 1 showing the correspondence between the two modal vectors. Where 0 indicates no correlation between the mode shapes, and 1 representing full correlation [19]. The MAC results for the tuned FE-model are presented by a colour plot in Figure 4-7, visualizing the correlation between the different eigenmodes from the initial tuning, where $K_r = 400\mathrm{N \cdot m}$.

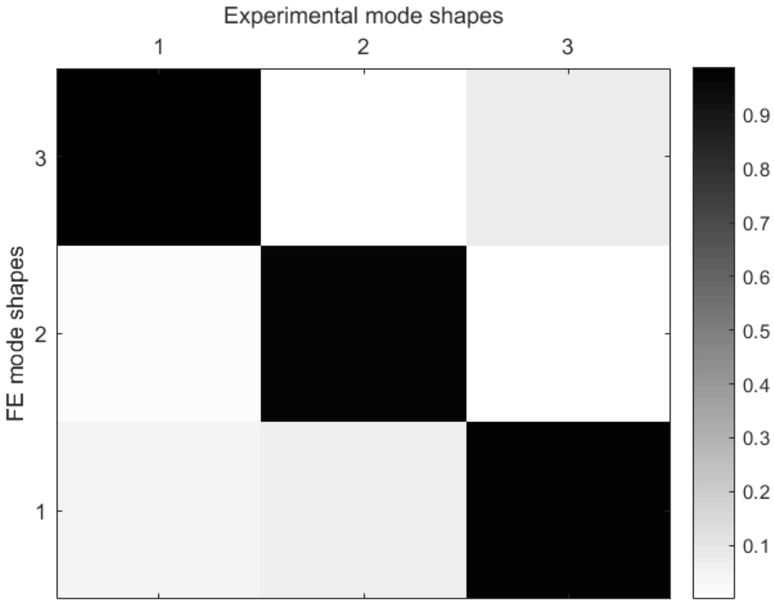

Figure 4-7: MAC values when comparing mode shapes from the tuned FE-model to the experimental.

Figure 4-7 shows the correlation between the different eigenmodes from the tuned FE-model and from the experimental modal analysis. The diagonal of Figure 4-7 illustrates almost full correlation between the first three in-plane eigenmodes from FE-model and experiment. To optimise the correlation of the eigenfrequencies and mode shapes between the FE-model and frame structure, an optimization is cast that searches by means of a genetic algorithm (GA).

4.3.3 Genetic Algorithm

Genetic coding is applied to obtain an FE-model which best resembles the modal parameters of the frame structure.

The Principle of Genetic Algorithm

The GA is a powerful optimization and search tool inspired by evolution [20] that enables the fittest candidates (solutions) to survive and reproduce based on random information search, imitating natural selection. The production of a new solution in the following generation uses information from the initial candidate, keeping the fittest candidates and hereby improving the search process [20], see Figure 4-8.

The GA provides a type of convergence, but not necessarily optimality, meaning multiple successive runs of GA will not necessarily produce the same solution for each run. The converged solution depends on which search space is chosen [20]. Some of the advantages of using GA are it allows the user to quickly scan for a solution through a solution set. As explained above, bad initial guess for a solution will not affect the result negatively since the bad solutions in the converging process are discarded. Also, since the GA searches for a solution through the entire model space, it is more likely to converge for a global solution, contrary a local optimization technique [20].

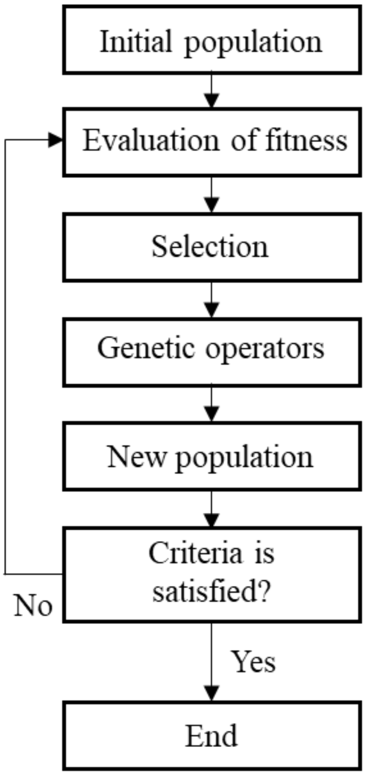

Figure 4-8: Activity diagram of GA process.

Implementation of GA

Using the integrated GA software in MATLAB as an optimization tool, the fittest tuning of the FE-model can be obtained. The GA software in MATLAB will use its converging methods to minimise a given function, J, with respect to the variable K_r. The challenge of using MATLAB's GA is to generate a function that minimises when the eigenfrequencies and mode shapes from FE-model and the experiment correlate. Using the MAC values from Eq. (4.5) and eigenfrequencies from Eq. (2.2) and EMA, a function J can be generated with respect to K_r.

$$J(K_r) = H_1 + H_2 \tag{4.6}$$

In Eq. (4.6) the variable H_1 and H_2 express the correlation between the modal parameters from the FE-model and EMA, and the objective is to define H_1 and H_2 such as the correlation increases when their value decreases.

$$H_1 = \sum_{i=1}^{n} \frac{|\omega_i - \widetilde{\omega}_i|}{\widetilde{\omega}_i} \tag{4.7}$$

Where:

ω_i, $\widetilde{\omega}_i$	are the eigenfrequency from the FE-model and experiment for i^{th} mode

The correlation between the three eigenfrequencies from the experiment and FE-model becomes higher when $H_1 \rightarrow 0$. A similar expression regarding the MAC values is made:

$$H_2 = \frac{1}{\sum_{i=1}^{n} MAC(i,i)} \tag{4.8}$$

Where:

$MAC(i,i)$ refers to the MAC value for i^{th} mode from the FE-model and experiment

It is clear to see from Eq. (4.7) and (4.8) that when the values of H_1 and H_2 become smaller, the correlation between the eigenmodes from the experiment and FE-model increases.

Choosing a search space, by defining a lower and upper limit[3], for the variable K_r, the GA function in MATLAB will then reduce the value of Eq. (4.6) as much as possible.

Table 4.4: Comparison of J-values regarding stiffness tuning using GA.

	Initial tuning $K_r = 400\mathrm{N \cdot m}$	GA tuning $K_r = 336\mathrm{N \cdot m}$	Deviation [%]
Value of function J	0.439	0.356	23.3

As it can be seen from Table 4.4 the value of J is reduced after implementation of GA. Using the new value for K_r should increase the correlation of the modal parameters between the FE-model and frame structure.

Table 4.5: Modal parameters obtained from initial tuning, GA tuning and EMA.

	Eigenfrequency [Hz]			MAC value [-]		
Initial tuning	11.91	40.06	79.27	0.989	0.964	0.977
GA tuning	11.39	38.66	77.37	0.988	0.960	0.974
EMA	11.39	39.09	77.14	-	-	-

As it can be seen from Table 4.5 the GA and initial tuning show a good correlation in mode shapes between the FE-model and frame structure, but the deviation in eigenfrequencies between the FEM-program and EMA is smaller after implementation of GA. Using the new K_r value for the stiffness tuning applicable shaped inputs are computed.

4.4 SUMMARY

To compute shaped inputs for experimental damage localisation, the modal parameters of the FE-model must correspond with the results obtained from the EMA in Section 3.4.2. This is done by implementing the extra mass contributions from the corner connections and accelerometers and introducing a GA optimization algorithm for stiffness tuning of the FE-model. This results in a higher correlation in modal parameters between the FE-model and frame structure, as illustrated in Table 4.4 and Table 4.5.

---

[3] The upper and lower limit for the genetic algorithm are chosen based on engineering judgement of previous examinations.

5 EXPERIMENTAL DAMAGE LOCALISATION

This section elaborates the experimental work conducted on the frame structure in regard to localise a mass perturbation using the SDLID method.

5.1 DATA ACQUISITION

The term data acquisition refers to the process of obtaining experimental data for further processing via acquisition software. For present thesis acceleration data are transferred to the Brüel and Kjær software LabShop, where the numerical data can be extracted or interpreted in time, frequency or Laplace domain.

When operating with data acquisition, an essential element to consider is the process of capturing the behaviour of the system, which is controlled by the sampling rate of the signal. The sampling rate indicates how many samples per second are measured by the software. To ensure adequate information is obtained from the accelerometers, the sampling time increment, defined in Eq. (5.1), must be sufficiently low.

$$\Delta t = \frac{1}{f_s} \qquad (5.1)$$

Where:

f_s sampling frequency

As it shows from Eq. (5.1) the sampling frequency, f_s, must be sufficiently high to capture the behaviour of the system.

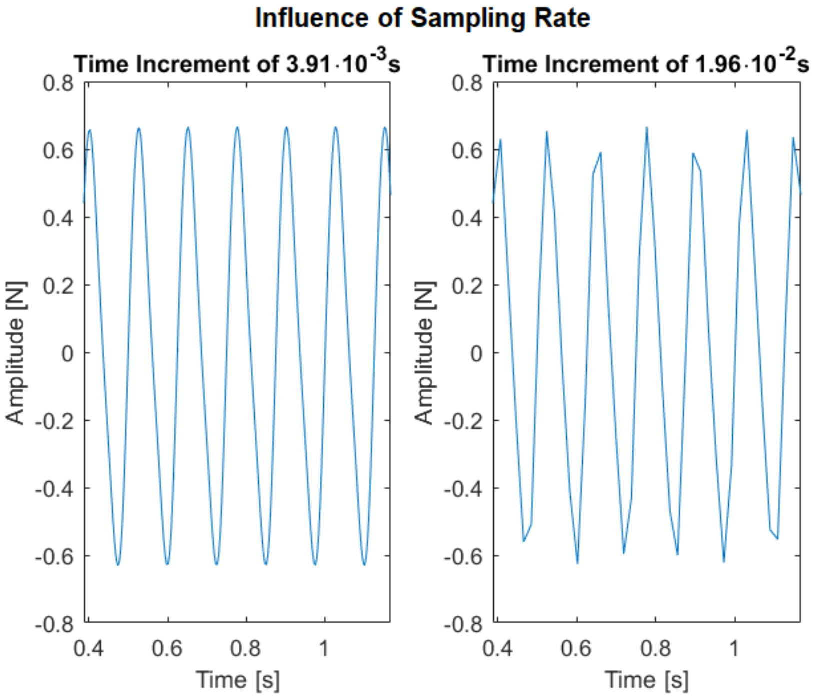

Figure 5-1: Force signal from an actuator with different sampling rate.

An example of a bad sampling rate is illustrated in Figure 5-1, where the same signal is plotted with two different time increments. It is clearly seen that setting the time increment to $1.96 \cdot 10^{-2}$s reduces the amount of information extracted from the signal. The total measurement time controls the frequency resolution, defined in Eq. (5.2).

$$\Delta f = \frac{1}{T} = \frac{f_s}{N} \tag{5.2}$$

Where:

T	total measurement time
N	number of measurements

As illustrated in Figure 5-1, setting the time increment to $3.91 \cdot 10^{-3}$s ensures that no valuable information is lost in the signal processing/data acquisition.

5.2 REFERENCE RESPONSE FOR DAMAGE LOCALISATION

This section elaborates how the response from an undamaged system (reference response) is obtained for the frame structure and then used for damage localisation.

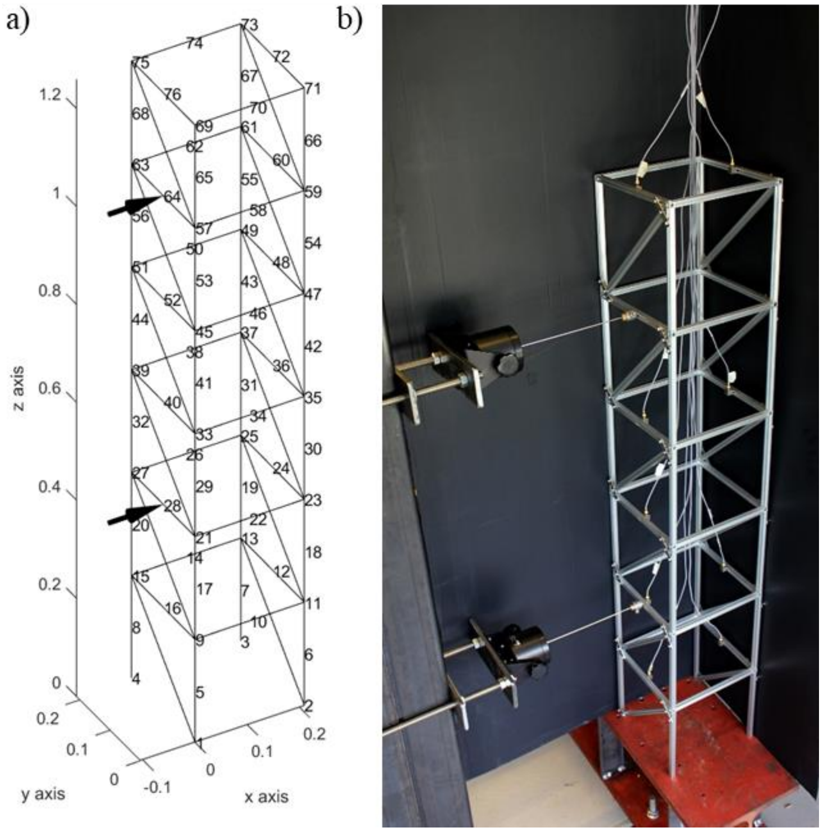

Figure 5-2: FE-model and experimental setup. a) Numerical model of the experimental setup with corresponding node numbers where the black arrows indicate location of shaped input. b) Experimental setup.

As it is depicted in Figure 5-2 only two actuators, or two shaped inputs, are present in the test setup, which in theory are not enough to suppress a node consisting of three translational DOF. The restriction against OOP bending from the braces results in only the translational DOF in the x-axis, defined in Figure 5-2, must actively be rendered dormant. To ensure that the frame structure will not enter a resonance state, the loading frequency for both actuators is chosen to be 70% of the first eigenfrequency (7.97Hz). In theory, every node in the structure should, and could, be rendered dormant. For present thesis six damage patterns are interrogated.

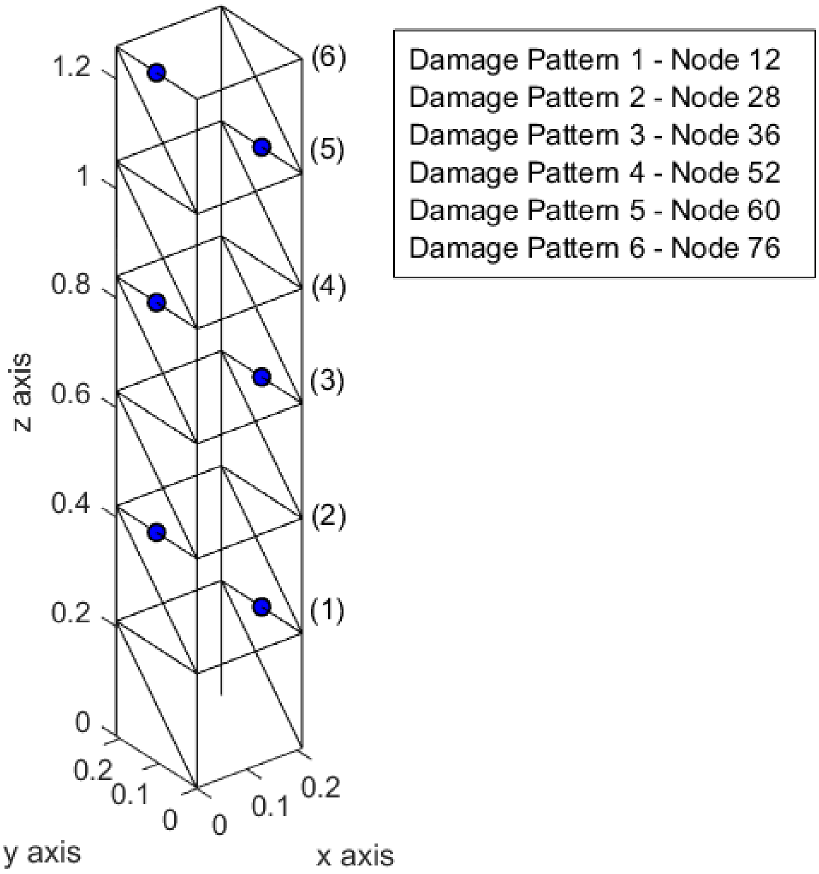

Figure 5-3: Location of damage patterns and the corresponding nodes.

The damage patterns are located at the front and rear side of the frame structure for each floor as illustrated in Figure 5-3. Using the tuned FE-model, obtained in Chapter 4, the shaped inputs, $\boldsymbol{f}_{\tau_i}(s)$, from each damage patterns are computed by finding the null space of $\boldsymbol{T}_i\boldsymbol{G}_{\bullet,\tau}(s)$ in Eq. (2.12). The amplitude and phase angle are configured for each actuator by computing the moduli and arguments of $\boldsymbol{f}_{\tau_i}(s)$.

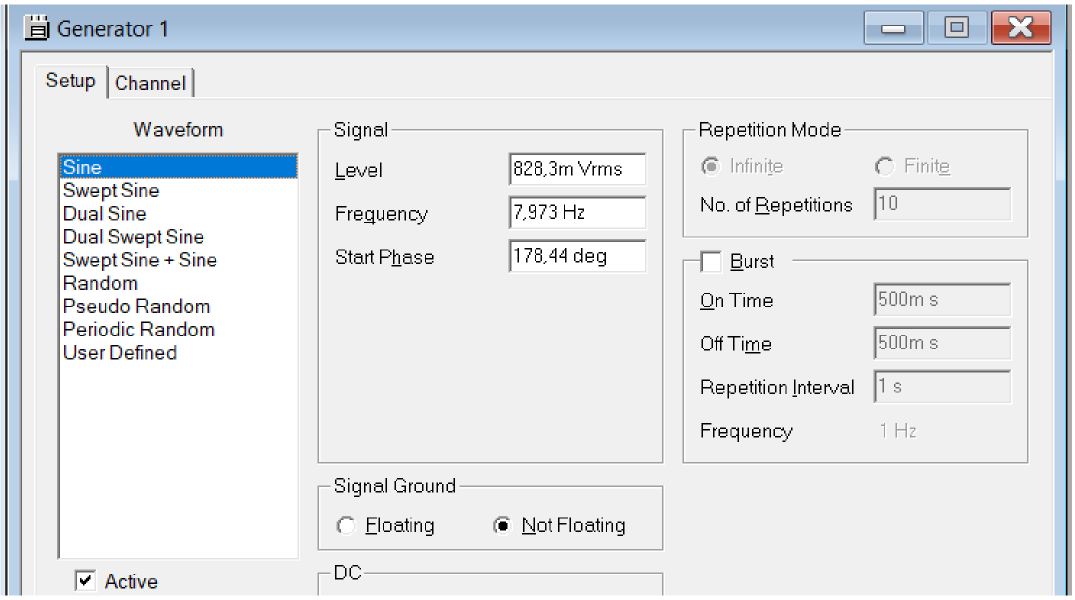

Generator 1

Setup | Channel

Waveform

- Sine
- Swept Sine
- Dual Sine
- Dual Swept Sine
- Swept Sine + Sine
- Random
- Pseudo Random
- Periodic Random
- User Defined

☑ Active

Signal

Level: 828,3m Vrms

Frequency: 7,973 Hz

Start Phase: 178,44 deg

Signal Ground

○ Floating ● Not Floating

DC

Repetition Mode

● Infinite ○ Finite

No. of Repetitions: 10

☐ Burst

On Time: 500m s

Off Time: 500m s

Repetition Interval: 1 s

Frequency: 1 Hz

Figure 5-4: Screenshot of programming the lowest positioned actuator for damage pattern 1 in LabShop.

Each actuator is configured in LabShop, such that all damage patterns are created by rendering the DOF in all specified nodes dormant. As it can be seen from Figure 5-4, the ratio between the amplitudes is controlled by adjusting the signal level for each actuator. To ensure that the transient part has damped out in the response, each test will last 64 seconds.

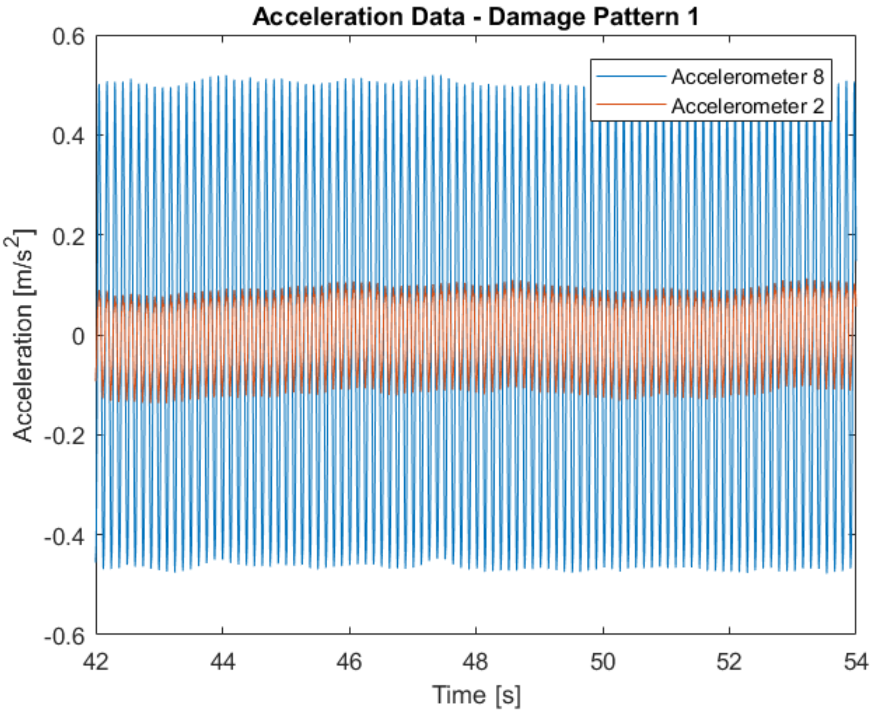

Figure 5-5: Accelerations from accelerometer 2 and 8 for damage pattern 1 (steady-state).

In Figure 5-5, an example of acceleration data from two sensors are shown, to illustrate that the data used for damage localisation only originates from steady-state. It is noticed that the response from accelerometer 2 is lower than accelerometer 8, this caused by the shaped inputs trying to render node 12 dormant, which is positioned on the same location as accelerometer 2.

In Section 2.4, the comparison between the reference and damaged response is done by taking the Euclidean distance between the two complex responses, but since the acceleration results are described in the time domain, the energy from the different responses are analysed instead by use of Fourier transformation.

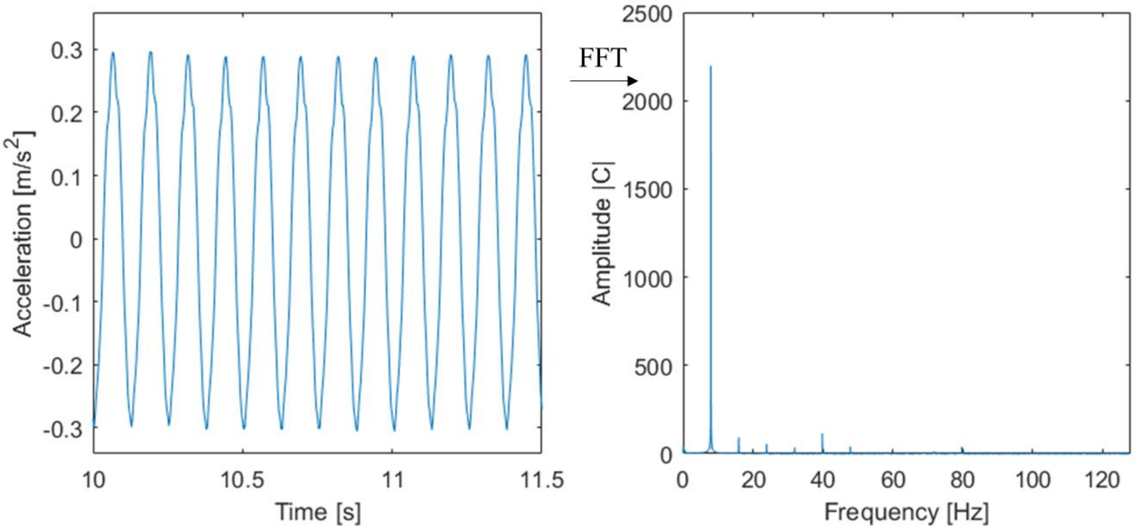

Figure 5-6: Accelerations and FFT plot of accelerometer 8 for damage pattern 3.

By describing the acceleration data in the frequency domain, the amplitude located at the loading frequency from the reference and damaged response are compared. Notice in Figure 5-6 that multiple peaks are present, besides the peak located at the loading frequency. These disturbances are due to imperfections in the actuator, amplifier and data processing. Only the amplitude peak located at the loading frequency (7.97Hz) is used for comparison with a response from a perturbated structure.

5.3 IMPLEMENTATION OF MASS PERTURBATION

In Section 2.3, numerical implementation of a mass perturbation is performed to validate the SDLID method. This section elaborates on how a mass perturbation is implemented on the frame structure and the considerations made.

Implementation of a mass perturbation for the experimental analysis is relatively straight forward. To show the robustness of the SDLID method the mass perturbation is implemented at five different locations on the frame structure. To localise the mass perturbations, using reference responses from Section 5.2 only the damage pattern’s locations are interrogated.

Figure 5-7: Implemented mass perturbation on frame structure for damage localisation in node 76, see Figure 5-2a.

As depicted in Figure 5-7, the mass perturbation is implemented using insulation tape to ensure that the mass is located as close to the node corresponding with the damage pattern as possible. Furthermore, the mass must be implemented firmly on the structure to minimise non-linear contributions during the tests and thereby corrupting test data. The implemented mass perturbation of 0.121kg is approximately 6.31% of the total mass of the frame structure.

5.4 DAMAGE DETECTION

Sine sweeps are conducted to see the effect the mass perturbation has on the modal parameters of the frame structure after damage implementation. The frequency interval used for the sine sweeps on the undamaged structure, described in Section 3.4.2., are reused.

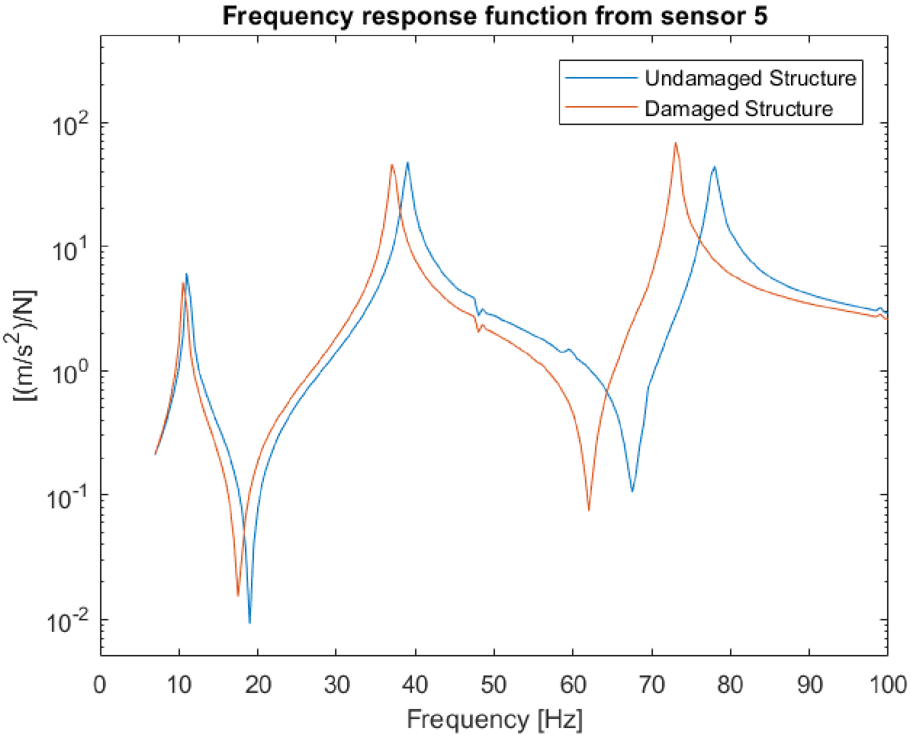

Figure 5-8: FRFs from damaged and undamaged structure.

As illustrated in Figure 5-8, the eigenfrequencies have clearly been reduced due to the mass perturbation in node 76. In practice analysing the shifts in eigenfrequencies can also be used as a damage detection method, as elaborated in Section 1.2. Table 5.1 shows relatively large eigenfrequency shifts between the undamaged and damaged structure, due to the large mass perturbation.

Table 5.1: Difference in eigenfrequencies of healthy and damaged structure.

Eigenmode	Damaged [Hz]	Undamaged [Hz]	Deviation [%]
Mode 1	10.7	11.4	6.54
Mode 2	37.2	39.1	5.11
Mode 3	73.0	77.1	5.62

5.5 DAMAGE LOCALISATION

Previous analysis indicated that damage is present on the structure, hence the SDLID method can be used for damage localisation in the same fashion as in Section 2.4. The same tests, conducted in Section 5.2, are performed on the damaged structure. Acceleration data are extruded from LabShop and presented in the frequency domain to compare the energy shift from the two structural states.

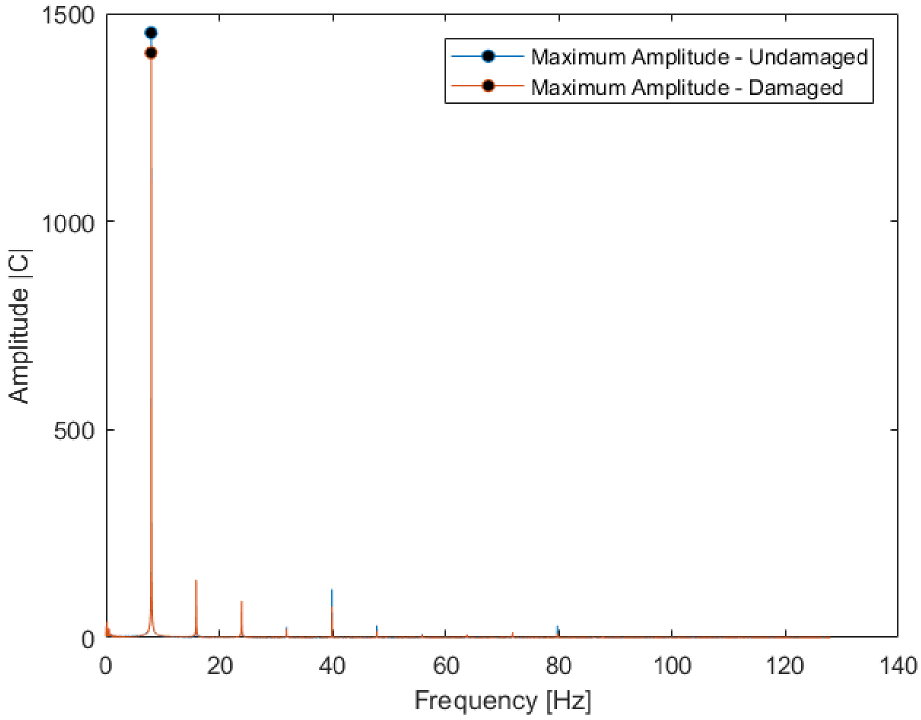

Figure 5-9: FFT plot of acceleration data from accelerometer 4, damage pattern 2.

From Figure 5-9 a clear change in amplitude is present when comparing the damaged and undamaged structure. This is caused by the energy shift from the mass perturbation.

Comparing the peaks at the loading frequency and summing up deviations from each accelerometer for each damage pattern, damage is localised, see Eq. (5.3), (5.4) and (5.5).

$$\Delta\boldsymbol{\Upsilon}^{(i)} = \boldsymbol{\Upsilon}_d^{(i)} - \boldsymbol{\Upsilon}_u^{(i)} \tag{5.3}$$

$$B^{(i)} = \sum_{j=1}^{\eta} \Delta\boldsymbol{\Upsilon}_j^{(i)} \tag{5.4}$$

$$\boldsymbol{B} = \begin{bmatrix} B^{(1)} \\ B^{(2)} \\ \vdots \\ B^{(d)} \end{bmatrix} \tag{5.5}$$

Where:

$\boldsymbol{B}$	damage indicator for ith damage pattern
$\boldsymbol{\Upsilon}_d, \boldsymbol{\Upsilon}_u$	vector containing peak amplitude of all accelerometers for damaged and undamaged state
d	number of damage patterns
η	number of accelerometers

The lowest value in the damage indicator vector, $\boldsymbol{B}$, should correspond with the damage pattern that renders the mass perturbation dormant. Thus, a damage pattern plot is made based on the results obtained using Eq. (5.5).

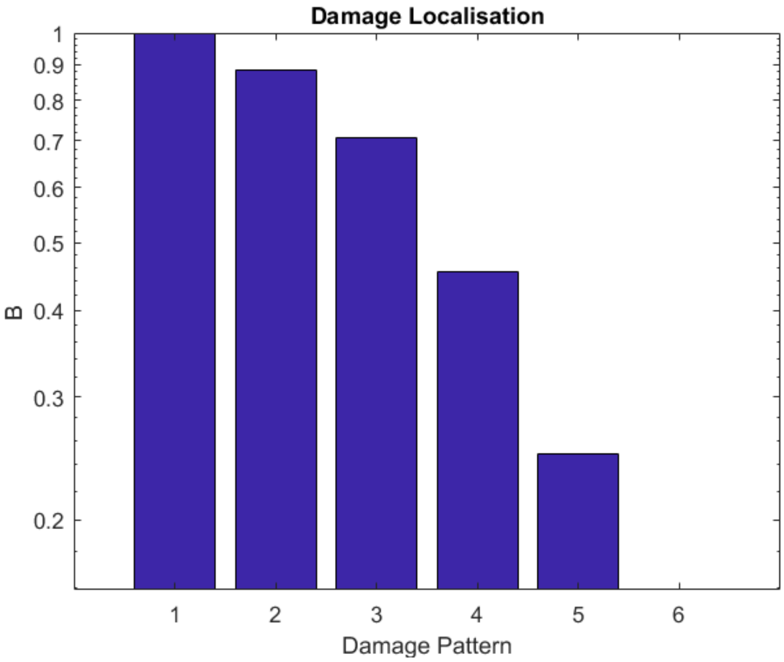

Figure 5-10: Damage pattern plot of damage located in node 76.

As depicted in Figure 5-10, the damage pattern plot clearly indicates the lowest deviation at damage pattern no. 6, which corresponds to node 76. Based on this result damage localisation in node 76 is possible. To test the robustness of the SDLID method, mass perturbations are implemented in node 12, 36, 52 and 60.

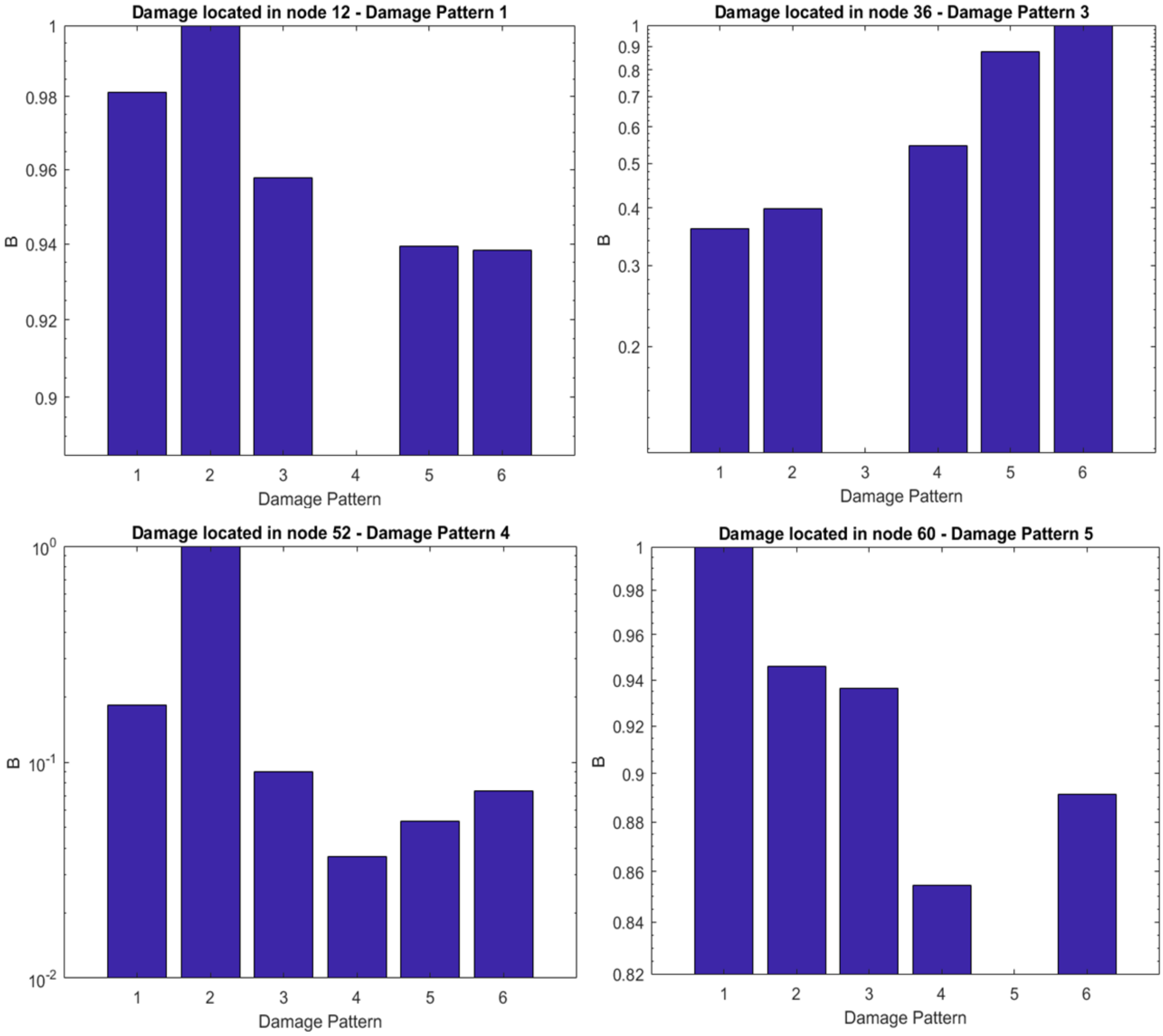

Figure 5-11: Damage pattern plot of various locations for mass perturbation.

As illustrated in Figure 5-11, all damage localisations are successful, except damage localisation in node 12. The plot shows the mass perturbation is located in node 52, which is not the case. This might be due to the location of the two actuators. To analyse if the location of shaped inputs is the explanation of the error-localisation, another test is performed where the actuators is placed in the 1st and 5th floor.

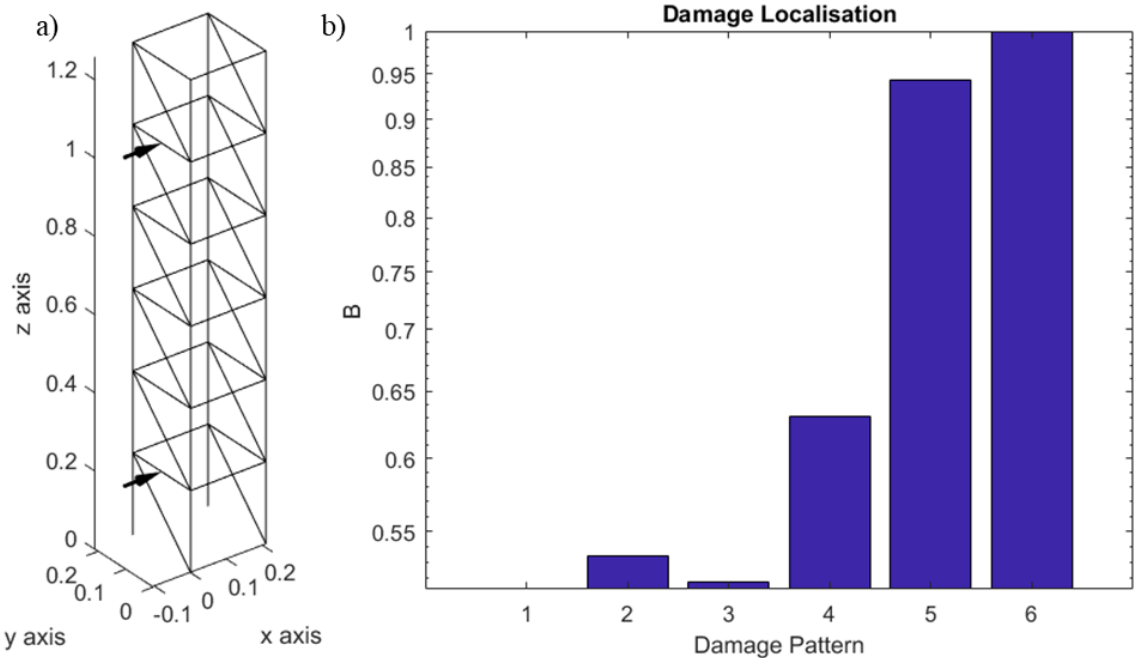

Damage Localisation

Figure 5-12: a) New location of shaped inputs. b) Damage pattern plot of mass perturbation in node 12.

From Figure 5-12b, there is an indication of a mass perturbation located in damage pattern 1 (node 12) despite the bad resolution. The results show that the placement of shaped inputs is important regarding damage localisation. The poor resolution in Figure 5-12 might be caused by the placement of the mass perturbation. Since it is located close to the boundary condition, the vibration signature, from the 1st floor, is not high enough to indicate the damage. Thereby, the measured responses from the highest placed accelerometers are similar to the reference response, giving an error in the localisation process.

5.5.1 Mass Magnitude Study

The previous damage localisation results are obtained with an added mass of 0.121kg, which is considered a relatively large mass perturbation, since it is 6.31% of the total mass of the frame structure. Therefore, a mass magnitude study regarding damage localisation is performed.

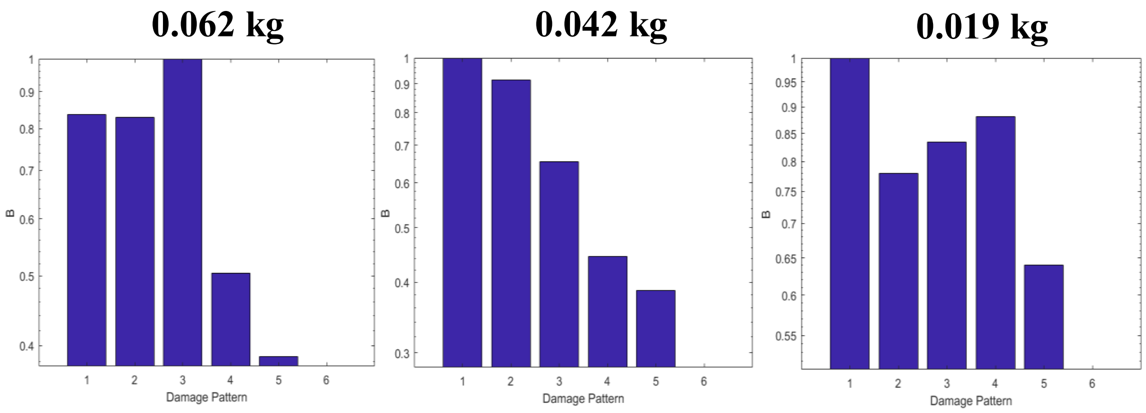
0.062 kg
0.042 kg
0.019 kg

Figure 5-13: Damage pattern plots for different mass perturbations located in node 76.

Using the same procedure as in Section 5.5 damage localisation in node 76 is performed with various masses. As illustrated in Figure 5-13, damages localisation is successful for all mass configurations.

5.6 SUMMARY

This chapter performs experimental analyses of the SDLID method. Damage localisation of a mass perturbation is performed on various locations on a frame structure to investigate the robustness of the SDLID method. Damage localisation in node 36, 52, 60 and 76, with the same shaped inputs placement, were successful. Based on the results presented in this chapter, localisation of a mass perturbation in node 12 showed complications, but a change in placement of the shaped inputs resulted in damage localisation, but with poor resolution.

6 DISCUSSION

This chapter discusses experiences and results from the conducted work during present thesis. Initially the advantages and drawbacks of the SDLID method are treated followed by a discussion of the experiences and results obtained from the experimental SDLID analyses. Assuming damage detection has taken place a priori, the method operates on postulating damage patterns and comparing responses from a reference and damaged structure.

Advantages

Operating on the premise of postulated damage patterns provides the merit of avoiding system identification, which is the largest merit of the SDLID method. Other advantages are robustness towards signal noise and that the method, in principle, can operate with only one well-placed output sensor. Robustness regarding damage localisation increases when implementing multiple sensors.

Drawbacks

Since the SDLID method operates on postulating damage patterns, steady-state responses from a reference and damaged structure must be obtained. This can be rather time consuming since the structure must be excited in a sufficient time period to ensure only steady-state responses are present. A complete search for mass and stiffness perturbations in the frame structure, discretised as in Figure 2-4, requires 360 responses. However, the practical necessity of performing every test can be argued, since interrogating for perturbation close to the damaged location will be noticeable in the nearby responses. Thereby the location of a damage can be indicated with fewer tests.

For the frame structure tested in present thesis, it is observed that the placement of actuators has a considerable influence regarding perturbation localisation. A further study of this behaviour is not discussed in present thesis.

6.1.1 Experimental Work Conducted with the SDLID Method

Following sections elaborate on error sources revealed by the experimental work, which showed to have a considerable influence on the ability to localise damage.

Calibrating the FE-model to Frame Structure

Experimental damage localisation is highly depended on an accurate FE-model of the structure in question, to create sufficiently accurate shaped inputs. An inaccurate FE-model can result in a low resolution or inability to localise the damage.

The deviation in the displacements presented in Table 3.4 is presumed to be caused by joint flexibility from the frame structure, which the initial FE-model does not take into consideration. Implementation of rotational springs, as described in Section 4.3, enables calibration of the FE-model to resemble the modal parameters for the frame structure. It is evaluated as a reasonable approximation to assign all rotational springs the same stiffness value, although physical differences are present. Calibration of rotational spring stiffness in the FE-model is performed with a GA against the experimentally measured first three in-plane eigenfrequencies and eigenmodes, which is evaluated as sufficient since the loading frequency, used for the experimental damage localisation tests, is beneath the first eigenfrequency of the frame structure.

Modelling the boundary conditions of the FE-model as fixed is evaluated as acceptable even though the connection between the frame structure and I-profile contains flexibility from the M3 threaded rod, washers and MakerBeam aluminium profile.

Damage Localisation

The experiments conducted show that mass damage localisation is possible. However, difficulties were revealed when interrogating for damage in node 12 on the frame structure, see Figure 5-11. It is presumed to emerge from the inability to “activate” the damage, caused by being located close to the fixation.

Mass Magnitude Study

The mass magnitude study, described in Section 5.5.1, investigates the influence for damage localisation when the size of the mass perturbation is reduced. As seen from the results in Figure 5-13, localisation of a mass perturbation of 0.019kg is performed, which is equivalent to approximately 1% of the frame structure’s total mass and is evaluated as satisfying regarding practical implementation of the SDLID method.

Location of Shaped Input

The importance of consistency in location of the shaped inputs was revealed during a set of tests, where the transducer-tip was re-mounted at the same floor, but presumably not the exact same position. This lead to differences in the reference responses, where those obtained before the re-mounting became unusable for damage localisation, hence new reference responses had to be obtained.

Real-life Implementation

Tests for present thesis are performed in a laboratory environment, which is considered well controlled. Performing tests on real-life structures, such as wind turbines and offshore foundations, includes taking several other factors into account such as: wind, temperature, sun/shade, which are expected to create challenges for the commercial implementation of the SDLID method.

7 CONCLUSION

This thesis presents a newly proposed method, Shaped Damage Locating Input Distribution (SDLID), for vibration-based damage localisation analysis by use of numerical analyses and experimental work. The first approach is performed to validate the damage localisation capabilities of the SDLID method by incorporating numerical models to simulate real-life conditions. The second approach is performed by conducting experimental tests of the SDLID method to investigate the validity for practical implementation of the method. Multiple tests are performed with various damage locations on a six-story frame structure to validate the SDLID method's capability in localising damages.

The idea behind the newly proposed SDLID method is to shape inputs at certain locations, such that specific steady-state vibration quantities are suppressed at one location at a time. Damage is located when the vibration signature from the damaged and undamaged structure correspond. The shaped inputs for the experimental tests are generated using the FE-model, which is tuned such it shares the same modal parameters as the frame structure.

The conclusion of this report is based on the numerical calculations and experimental work performed on the frame structure. The numerical analyses validated the premise of the SDLID method by use of 2D and 3D FE-models. The experimental work showed that implementation of shaped inputs facilitates acceptable damage localisation, when applying a harmonic load, with a frequency equal to 70% of the frame structure's first eigenfrequency. Despite inaccuracy in the FE-model tuning and uncertainties regarding the fixation of the frame structure, it is accomplished to localise mass perturbations between 0.019-0.121kg (where 0.019kg being approximately 1% of the frame structure's total mass). Damage localisation in 1st floor showed complications, which is presumed to arise from the small dynamic impact from the mass perturbation on to the frame structure. Moving the shaped inputs/actuators resulted in more satisfying localisation results but with relatively poor resolution.

8 BIBLIOGRAPHY

[1] T. Moan, “The Alexander L. Kielland Accident,” Swa Grant College Program & Department of Ocean Engineering Massachusetts Institute of Technology, Cambridge, 1981.

[2] Officer of The Watch, “officerofthewatch.com,” 29 04 2013. [Online]. Available: https://officerofthewatch.com/2013/04/29/alexander-l-kielland-platform-capsize-accident/. [Accessed 18 12 2017].

[3] M. D. Ulriksen, D. Tcherniak and L. Damkilde, “Damage detection in an operating Vestas V27 wind turbine blade by use of outlier analysis,” Aalborg University, Esbjerg, 2015.

[4] FoundOcean, “www.foundocean.com,” [Online]. Available: http://www.foundocean.com/en/what-we-do/products/marine-growth-prevention/. [Accessed 27 10 2017].

[5] C. R. Farrar, S. W. Doebling and D. A. Nix, “Vibration-Based Structural Damage Identification,” *The Royal Society Publishing,* p. 19, 2001.

[6] A. Rytter, “Vibrational Based Inspectiom of Civil Engineering Structures,” Department of Bulding Technology and Structural Engineering, Aalborg, 1993.

[7] J. Runyon, “How Drones Will Transform Wind Turbine Inspections,” *Renewable Energy World,* p. 4, 7 December 2017.

[8] S. W. Doebling, C. R. Farrar, M. B. Prime and D. W. Shevitz, “Damage Identification and Health Monitoring of Structural and Mechanical Systems from Changes in Their Vibration Characteristics: A Literature Review,” Los Alamos: National Laboratory, Los Alamos, New Mexico, 1996.

[9] D. Bernal, “Damage Localization from the Null Space of Changes in the Transfer Matrix,” *AIAA Journal,* p. 8, 2 February 2007.

[10] M. D. Ulriksen, “Input control for damage localization,” in *Damage Localization for Structural Health Monitoring,* Aalborg, Aalborg University Press, 2017, pp. 53 - 60.

[11] MakerBeam, “makerbeam.com,” MakerBeam, [Online]. Available: https://www.makerbeam.com/makerbeam/. [Accessed 22 09 2018].

[12] D. J. Inman, Engineering Vibration, Fourth edition ed., Essex: Pearson Education Limited, 2014.

[13] R. D. Cook, D. S. Malkus, M. E. Plesha and R. J. Witt, Concepts and Application of Finite Element Analysis, 4. ed., Hoboken, NJ 07030, USA, New Jersey: John Wiley & Sons, Inc., 2002.

[14] MakerBeam, “makerbeam.com,” [Online]. Available: https://drive.google.com/drive/folders/0B8h5C_ek_fmKc3BFOGVnYmRpVDQ. [Accessed 15 11 2017].

[15] Brüel & Kjær, “www.bksv.com,” [Online]. Available: https://www.bksv.com/-/media/literature/Product-Data/bp0232.ashx. [Accessed 23 11 2017].

[16] Brüel & Kjær, “www.bksv.com,” [Online]. Available: https://www.bksv.com/en/products/transducers/vibration/Vibration-transducers/force-transducers/8230-001. [Accessed 23 11 2017].

[17] Brüel & Kjær, “www.bksv.com,” Brüel & Kjær, [Online]. Available: https://www.bksv.com/en/products/transducers/vibration/Vibration-transducers/accelerometers/4507-B. [Accessed 23 11 2017].

[18] O. Døssing, “bksv.com,” [Online]. Available: https://www.bksv.com/media/doc/br0507.pdf. [Accessed 12 03 2018].

[19] M. Pastor, M. Binda and T. Harčarik, “Modal Assurance Criterion,” Technical University of Košice of Mechanical Engineering, Košice, 2012.

[20] S. Sumathi, T. Hamsapriya and P. Surekha, Evolutionary Intelligence - An Introduction to theory and applications with Matlab, Coimbatore: Springer, 2008.

[21] Brüel & Kjær, “www.bksv.com,” [Online]. Available: https://www.bksv.com/-/media/literature/Product-Data/bp2078.ashx. [Accessed 23 11 2018].

[22] Vernier, “www.vernier.com,” [Online]. Available: https://www.vernier.com/manuals/3d-bta/#section6. [Accessed 06 12 2017].

9 APPENDIX

Content

9.1 APPENDIX A - MODAL ANALYSIS: OUT OF PLANE & TWISTING

Since only in-plane eigenmodes are of interest in present thesis, it is tested if any twisting and/or out of plane (OOP) eigenmodes are present beneath 100Hz. Two impulse tests are performed, one with the Brüel & Kjær equipment and another with a LoggerLite 3-axis accelerometer, depicted in Figure 9-4. Advantages and disadvantages are listed below, regarding impulse testing, followed by a description of the equipment used.

Advantages using impulse excitation:

- No additional mass is added to the structure
- Faster to conduct, portable and easy setup compared to sine sweep
- Often low signal to noise ratio

Disadvantages using impulse excitation:

- Large structures require a larger impulse, which can be hard to obtain without damaging the structure (locally)
- Risk for double impacts
- Not suitable for non-linear problems

Since the actuators are difficult to move into OOP excitation, impulse test is used to establish modal parameters for OOP bending and twisting of the frame structure.

9.1.1 Out of Plane Impulse Excitation - Brüel & Kjær

Impulse excitation of the frame structure is done with an impulse hammer, depicted in Figure 9-1, which measures the impulse applied to the frame structure and hereafter transfers it to the PulseReflex software.

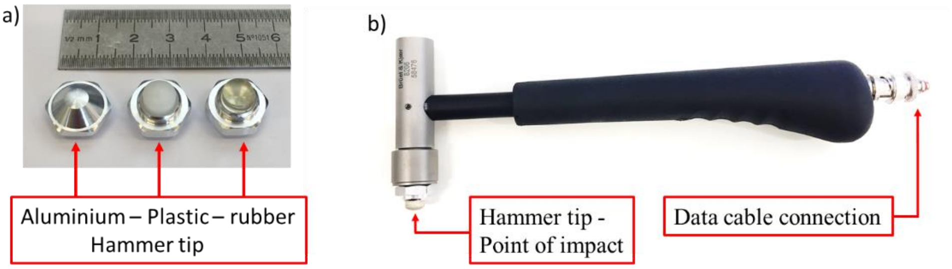

Figure 9-1: Impulse excitation equipment. a) Three hammer tips with different hardness. b) Brüel & Kjær Impact Hammer Type 8206 [21].

The impulse hammer is supplied with three different hammer tips: aluminium, plastic and rubber, depicted in Figure 9-1a, where a harder tip can excite higher frequencies, which are illustrated in Figure 9-2.

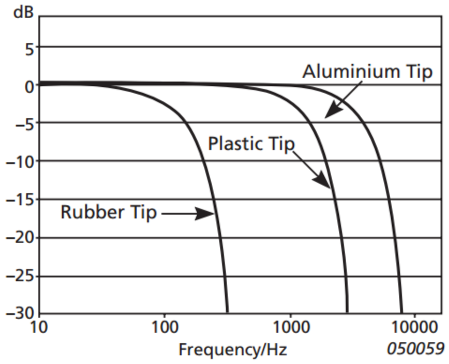

Figure 9-2: Associated bandwidth for impact on an aluminium-plate [21].

Since the frame structure’s third eigenfrequency is approximately 77Hz, see Figure 3-9, the rubber tip is used.

The advantages of impulse excitation, in contrast to harmonic excitation, is that no additional damping is applied to the structure in question and that the signal to noise ratio (SNR) usually is satisfying due to the nature (free decay) of the output.

Table 9.1: Impact Hammer Type 8206 selected data [21]:

Characteristic	Value
Maximum force	220 [N]
Linear error at full scale	<± 0.01

Measuring Impulse Force & FRF

The impulse applied to the structure by the impact hammer is measured inside the hammer head and transferred to the PulseReflex software for processing. In combination with output from the accelerometers, the frequency response functions are calculated and depicted in Figure 9-3.

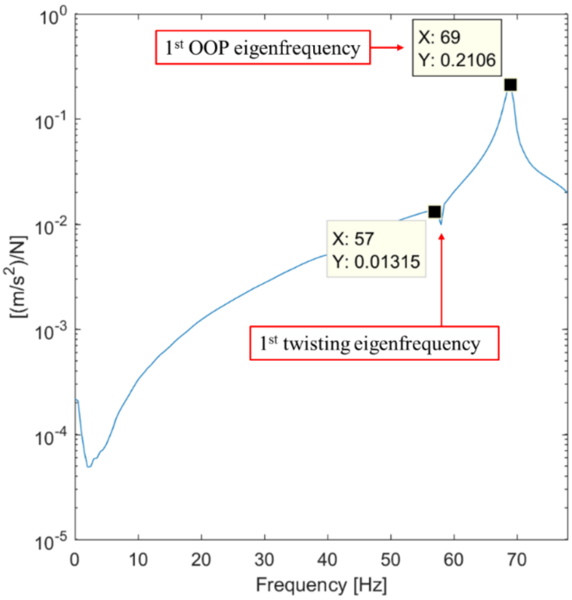

Figure 9-3: OOP impulse test with uniaxial Brüel & Kjær accelerometers.

Figure 9-3 indicates an OOP eigenfrequency at approximately 69Hz. The bump in the curve around 57Hz is evaluated as interference from the first twisting and in-plane mode respectively.

9.1.2 Out of Plane Impulse Excitation - LoggerLite

The LoggerLite 3D-BTA accelerometer [22], depicted inFigure 9-4, is positioned on the frame structure as depicted in Figure 9-7a. The experiment is not taking the extra mass of 0.020kg into account of the LoggerLite accelerometer, which is evaluated as negligible in this context.

Figure 9-4: 3-axis accelerometer model “LoggerLite 3D-BTA”.

The frame structure is given an impulse with a hammer in the OOP direction, to excite the OOP and twisting eigenmodes. Due to the braces contributing to extra stiffness in the OOP axis, the impulse excitation will initially excite the frame structure in the OOP direction, before the energy transfer will cause the vibrations to become primarily in the weaker in-plane direction, hence this requires less energy. This is also seen from the blue (in-plane) and red (OOP) curves in Figure 9-6.

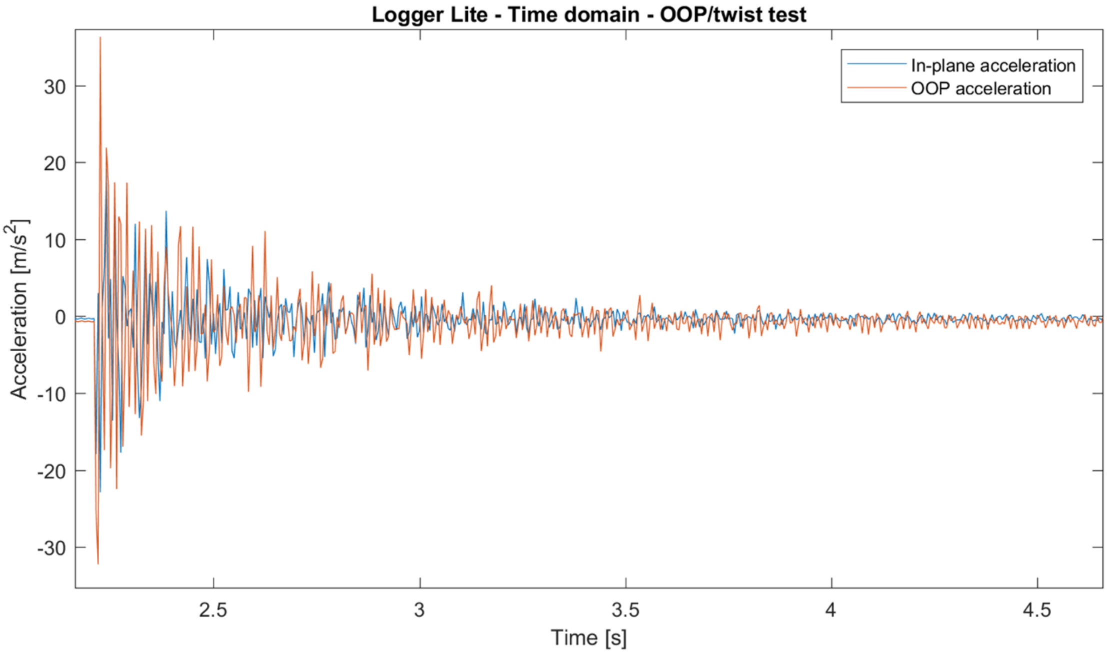

Figure 9-5: Section of acceleration data from OOP impulse excitation.
Blue line: in-plane accelerations. Red line: OOP accelerations (vertical accelerations omitted).

Eigenfrequencies – Out of Plane and Twisting

From the red curve in Figure 9-6, it is seen that the first OOP eigenfrequency is approximately 69Hz. As expected, the blue curve peaks at the in-plane eigenfrequencies and together with the red curve at the twisting eigenfrequency, see Section 3.4.2.

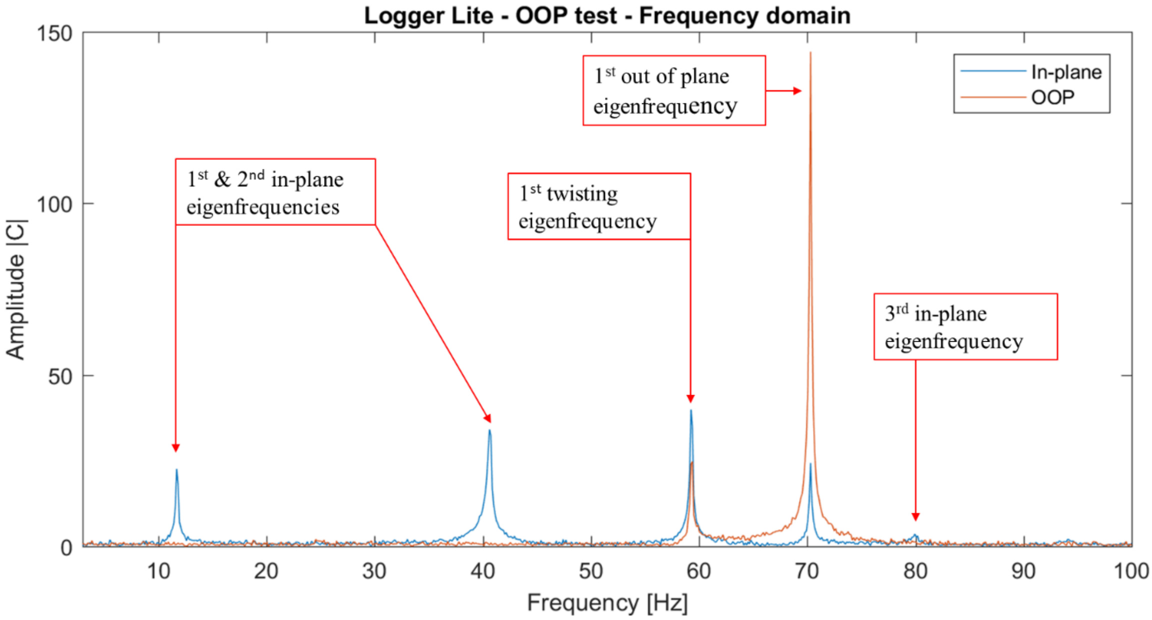

Figure 9-6: FFT plot from impulse excitation. Blue line: in-plane eigenfrequencies. Red line: OOP eigenfrequencies.

Eigenfrequency - Twist

Determining a twisting mode for the frame structure is illustrated in Figure 9-7b, where it is seen the x- and y-distances from origo to the accelerometer are equal, giving that when their accelerations are similar, it is a twisting mode.

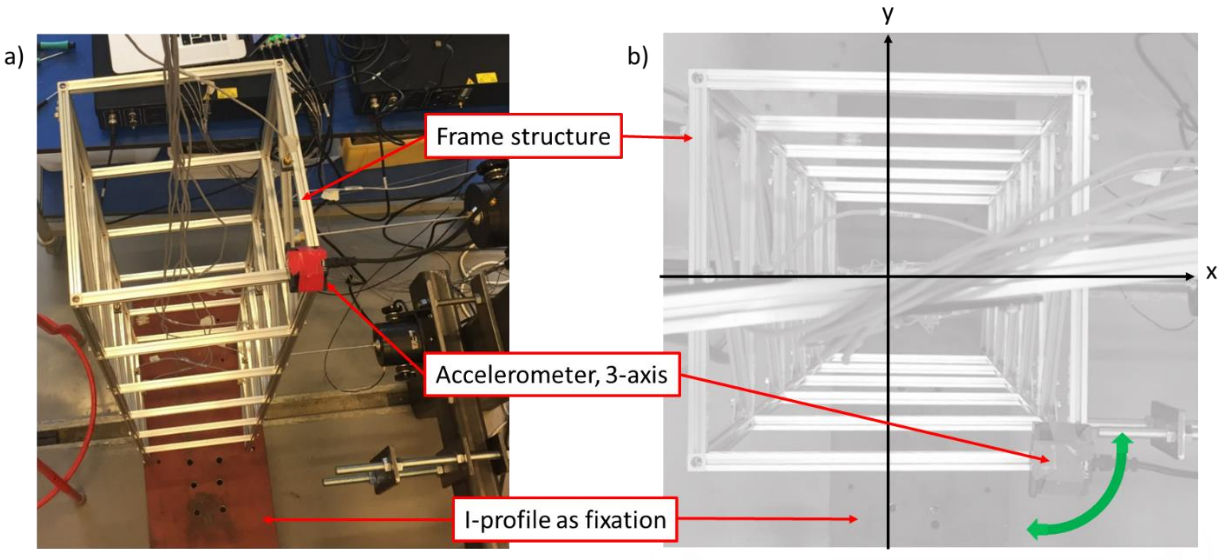

Figure 9-7: a) Side/top view of frame structure with LoggerLite accelerometer fixed on top corner. b) Top view of frame structure with coordinate system. Green arrow indicating twisting mode.

The eigenfrequency for the first twisting eigenmode is approximately 57Hz, as seen in Figure 9-6. Based on the results presented in Appendix A, it is concluded that the frame structure’s first twisting and OOP eigenfrequency are at approximately 57Hz and 69Hz, respectively, which explains the small peaks in the curves in Figure 3-9 presented in the thesis.

9.2 APPENDIX B - FINITE ELEMENT METHOD

The frame structure used for the laboratory test is constructed of MakerBeam aluminium elements as illustrated in Figure 2-3c and d. The relative slender and open profile of the MakerBeam elements leads to the assumption that shear forces are negligible. Detailed modelling of the beam connections, depicted in Figure 3-1, where the M3 threaded rods are considered as differently pretensioned springs, is omitted. This leads to following two assumptions:

- A FE-model on basis of Bernoulli-Euler beam theory.
- Handling the divergent properties of the connections, by implementation of rotational springs into the FE-model, are elaborated in the thesis in Section 4.3.

Following sections gives a brief description on calculation of local stiffness, mass and rotation matrices and assembling into a global matrix in 2D [13].

Local Stiffness Matrix

A local stiffness matrix consists of values for each DOF in an element of the numeric model. The DOF for a single 2D Bernoulli-Euler beam element are illustrated in Figure 9-8. It consists of two nodes where the interaction to neighbouring elements is transferred to the three DOF at each node.

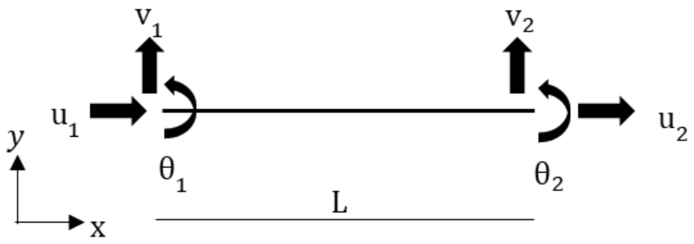

Figure 9-8: Illustration of a 2D beam element and its associated DOF.

Where:

u_x, v_x, θ_x represent translational and rotational DOF

The values for each DOF represents the stiffness towards translational and rotational displacement. The values for translational and rotational displacement are derived from the constitutive law in Eq. (9.1):

$$\frac{\partial^2 v(x)}{\partial x^2} = \frac{M(x)}{EI} \tag{9.1}$$

Where:

E, I modulus of elasticity and moment of inertia

$M(x)$ curvature with respect to x

The transverse stiffness value at node v_1 is obtained by giving it a displacement of one and the other DOF a displacement of zero, as illustrated in Figure 9-9.

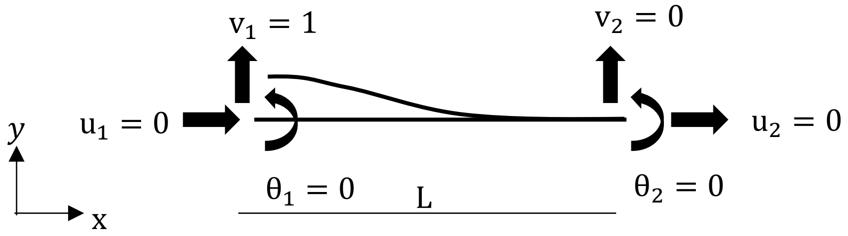

Figure 9-9: Transverse displacement set to 1. All others DOF are set to 0.

$v_1 = 1$ substituted into Eq. (9.1) gives:

$$\theta(x) = \frac{\partial v(x)}{\partial x} = \int \frac{-M_1 + V_1 x}{EI} dx = -\frac{M_1 x}{EI} + \frac{V_1 x^2}{2EI} + \frac{c_1}{EI} \tag{9.2}$$

$$v(x) = \int \int \frac{-M_1 + V_1 x}{EI} dx = -\frac{M_1 x^2}{2EI} + \frac{V_1 x^3}{6EI} + \frac{c_1 x}{EI} + \frac{c_2}{EI} \tag{9.3}$$

Boundary conditions are implemented:

$$\theta_1 = \theta(0) = \frac{c_1}{EI} = 0 \rightarrow c_1 = 0$$

$$v_1 = v(0) = \frac{c_2}{EI} = 1 \rightarrow c_2 = EI$$

Substituting above into Eq. (9.2) and Eq. (9.3), results in expressions for k_{22}, $k_{23}\ and\ k_{32}$. The remaining values are computed with the same approach. The local stiffness matrix with all stiffness contributions are shown in Eq. (9.4):

$$[\boldsymbol{K}_{local}] = \begin{bmatrix} \frac{EA}{L} & 0 & 0 & -\frac{EA}{L} & 0 & 0 \\ 0 & \frac{12EI}{L^3} & \frac{6EI}{L^2} & 0 & -\frac{12EI}{L^3} & \frac{6EI}{L^2} \\ 0 & \frac{6EI}{L^2} & \frac{4EI}{L} & 0 & -\frac{6EI}{L^2} & \frac{2EI}{L} \\ -\frac{EA}{L} & 0 & 0 & \frac{EA}{L} & 0 & 0 \\ 0 & -\frac{12EI}{L^3} & -\frac{6EI}{L^2} & 0 & \frac{12EI}{L^3} & -\frac{6EI}{L^2} \\ 0 & \frac{6EI}{L^2} & \frac{2EI}{L} & 0 & -\frac{6EI}{L^2} & \frac{4EI}{L} \end{bmatrix} \tag{9.4}$$

Rotation Matrix

Modelling elements rotated relative to the global x-axis requires a rotation matrix to adjust the values in the local stiffness matrix accordingly, which is illustrated in Figure 9-10.

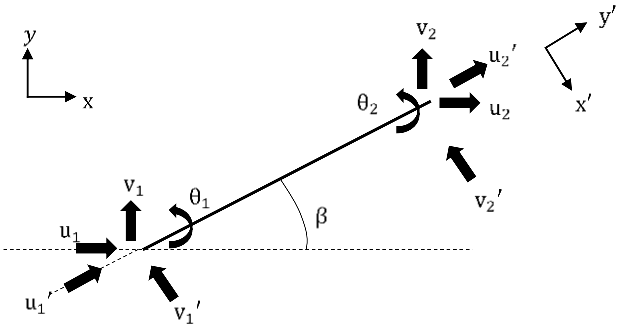

Figure 9-10: Rotation of a 2D beam element. Local DOF: u_x‘, v_x‘.
Global DOF: u_x, v_x.

To obtain a global stiffness matrix that operates on DOF referred to global coordinates, a rotational coordinate transformation to $\boldsymbol{K}_{local}$ is applied, shown in Eq. (9.7).

$$\boldsymbol{R}_{node} = \begin{bmatrix} c & s & 0 \\ -s & c & 0 \\ 0 & 0 & 1 \end{bmatrix} \quad c = cos(\beta) \ \wedge \ s = sin(\beta) \tag{9.5}$$

R_{node} is inserted into the R matrix as in Eq. (9.6):

$$\boldsymbol{R} = \begin{bmatrix} R_{node} & 0 \\ 0 & R_{node} \end{bmatrix} \tag{9.6}$$

Implementation to global coordinates is done by applying $\boldsymbol{R}$ to $\boldsymbol{K}_{local}$ as in Eq. (9.7):

$$\boldsymbol{K}_{beam,i} \ = \boldsymbol{R}^T \boldsymbol{K}_{local,i} \, \boldsymbol{R} \tag{9.7}$$

Global Stiffness Matrix

Local stiffness matrices, $\boldsymbol{K}_{local}$, computed for each beam, $\boldsymbol{K}_{beam,i}$, are assembled into a global stiffness matrix, $\boldsymbol{K}_{global}$, that represents the stiffness of the entire FE-model, as depicted in Figure 9-11.

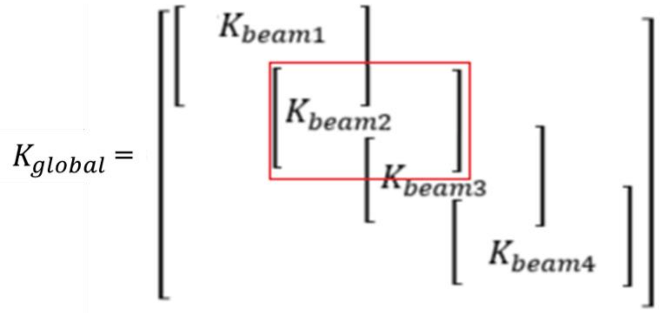

Figure 9-11: Principle in assembling several local matrices into one global matrix.

If a node is connecting with several elements, the values from the local stiffness matrices are summed in the global stiffness matrix at the corresponding DOF.

Local Mass Matrix

For the frame structure a consistent mass matrix is chosen giving each element at local mass matrix as shown in Eq. (9.8):

$$[\boldsymbol{M}_{local}] = \frac{\rho A L}{420}\begin{bmatrix} 140 & 0 & 0 & 70 & 0 & 0 \\ 0 & 156 & 22L & 0 & 54 & -13L \\ 0 & 22L & 4L^2 & 0 & 13L & -3L^2 \\ 70 & 0 & 0 & 140 & 0 & 0 \\ 0 & 54 & 13L & 0 & 156 & -22L \\ 0 & -13L & -3L^2 & 0 & -22L & 4L^2 \end{bmatrix} \tag{9.8}$$

Where:

ρ, A, L density, cross section area and element length

Thereby representing the total mass of each element.

Global Mass Matrix

Assembly of local mass matrices into a global mass matrix is similar to assembling the global stiffness matrix.

9.2.1 FEM 3D

The same principles for 2D FEM are used for 3D FEM, where the number of DOF are expanded to 6 for each node, thereby changing the rotation matrix and expanding local matrices $\boldsymbol{M}, \boldsymbol{K}$ and $\boldsymbol{C}$ into 12x12 matrices. For a thorough elaboration on 3D FEM is referred to [13].